nature methods

ARTICLES

https://doi.org/10.1038/s41592-020-0883-z

Mid-infrared metabolic imaging with vibrational probes

Lixue Shi[1], Xinwen Liu[1,7], Lingyan Shi[1,5,7], H. Ted Stinson[2], Jeremy Rowlette[2], Lisa J. Kahl[3], Christopher R. Evans[3], Chaogu Zheng[3,6], Lars E. P. Dietrich[3] and Wei Min[1,4]✉

Understanding metabolism is indispensable in unraveling the mechanistic basis of many physiological and pathological processes. However, in situ metabolic imaging tools are still lacking. Here we introduce a framework for mid-infrared (MIR) metabolic imaging by coupling the emerging high-information-throughput MIR microscopy with specifically designed IR-active vibrational probes. We present three categories of small vibrational tags including azide bond, ^{13}C-edited carbonyl bond and deuterium-labeled probes to interrogate various metabolic activities in cells, small organisms and mice. Two MIR imaging platforms are implemented including broadband Fourier transform infrared microscopy and discrete frequency infrared microscopy with a newly incorporated spectral region (2,000–2,300 cm^{-1}). Our technique is uniquely suited to metabolic imaging with high information throughput. In particular, we performed single-cell metabolic profiling including heterogeneity characterization, and large-area metabolic imaging at tissue or organ level with rich spectral information.

Genetics and metabolism are two defining characteristics of life. Indeed, understanding metabolism is indispensable in unraveling the mechanistic basis of many biological processes, such as development, homeostasis and response to stimuli[1–3]. After all, it is the synthesis, transformation and degradation of biomolecules (that is, metabolism) inside each cell that carry out the genetic blueprint. Besides physiology, metabolism also plays a key role in many diseases, including neurodegenerative diseases[4], diabetes[5] and cancer[6].

Despite the importance of metabolism, imaging tools to map in situ metabolic activities are relatively limited. Magnetic resonance spectroscopy and positron emission tomography lack sufficient spatial resolution to obtain cellular information[7]. Fluorescence microscopy offers subcellular resolution but requires bulky fluorophore labeling, which is often perturbative to metabolite functions in vivo. Mass spectrometry imaging is destructive and requires a long analysis time[8]. Raman microscopy, especially the emerging stimulated Raman scattering (SRS), coupled with Raman-active probes has opened up a broad range of applications of metabolic imaging[9–16]. Unfortunately, Raman-based metabolic imaging is limited by the extremely small Raman cross section at the level of ~10^{-30}–10^{-28} cm^2. As a result, the achievable information throughput of Raman technique is still far from ideal, because of either slow imaging speed or limited spectral coverage.

Here we offer an alternative approach to metabolic imaging by performing mid-infrared (MIR) microscopy coupled with IR-active probes. A key premise is that IR absorption cross sections are about 10^{10} times larger than their Raman couterparts[17–19]. More importantly, driven by two main technologies, MIR microscopy has undergone a rapid revolution in instrumentation toward high-information throughput. On the detector side, multi-pixel detectors known as a focal plane array (FPA) have revolutionized the use of Fourier transform IR (FTIR) imaging[20]. On the light-source side, high-power quantum cascade lasers (QCL) render a new model called discrete frequency MIR (DFIR) imaging with video-rate acquisition speed[21,22]. However, the prevailing example in MIR microscopy is label-free imaging. Very few attempts were reported under low-throughput modality with deuterated fatty acids[23,24] or metal carbonyls[25]. Leveraging high-information-throughput MIR microscopy, we introduced a set of specifically designed probes to demonstrate applications along single-cell metabolic profiling and large-scale tissue metabolic imaging. Beyond FTIR and DFIR, our framework can be readily translated to other MIR imaging schemes.

Design of IR-active probes for metabolic imaging in cells, small organisms and mice

Several IR-active moieties such as metal carbonyl and nitriles have been studied as vibrational probes with IR spectroscopy[18,26,27]. They are particularly useful as reporters of local environment such as the electric field inside biomolecules[19]. Although the concept of IR probes has been around in the spectroscopy literature, they are rarely explored for metabolic imaging especially to study animal physiology. Herein, we propose three categories of small vibrational tags for metabolic tracking of various pathways including azide bond, ^{13}C isotope-edited carbonyl bond and deuterium-labeled probes.

The azide bond is a desirable IR tag for a specific metabolite. It exhibits a single, narrow and strong IR band in the cell-silent window (Fig. 1a). Its large molar extinction coefficient (ε) about 400 M^{-1} cm^{-1} (ref. [18]) corresponds to a cross section of 1.5×10^{-18} cm^2, which is ten orders higher than the Raman scattering cross section of alkyne bonds. Moreover, azide is chemically inert and nearly absent inside cells, hence the bioorthogonality. Indeed, many azide-labeled precursors have been established for bioorthogonal chemistry, in which alkyne-fused probes can react with the azide functional group, proving their minimal toxicity and high biocompatibility in vivo[28]. Here we demonstrate the use of the azide tag for MIR metabolic imaging by using an azide-tagged methionine analog, azidohomoalanine (AHA) and an azide-labeled palmitic

[1]Department of Chemistry, Columbia University, New York, NY, USA. [2]Daylight Solutions Inc., San Diego, CA, USA. [3]Department of Biological Sciences, Columbia University, New York, NY, USA. [4]Kavli Institute for Brain Science, Columbia University, New York, NY, USA. [5]Present address: Department of Bioengineering, University of California San Diego, La Jolla, CA, USA. [6]Present address: School of Biological Science, The University of Hong Kong, Hong Kong, China. [7]These authors contributed equally: Xinwen Liu, Lingyan Shi. ✉e-mail: wm2256@columbia.edu

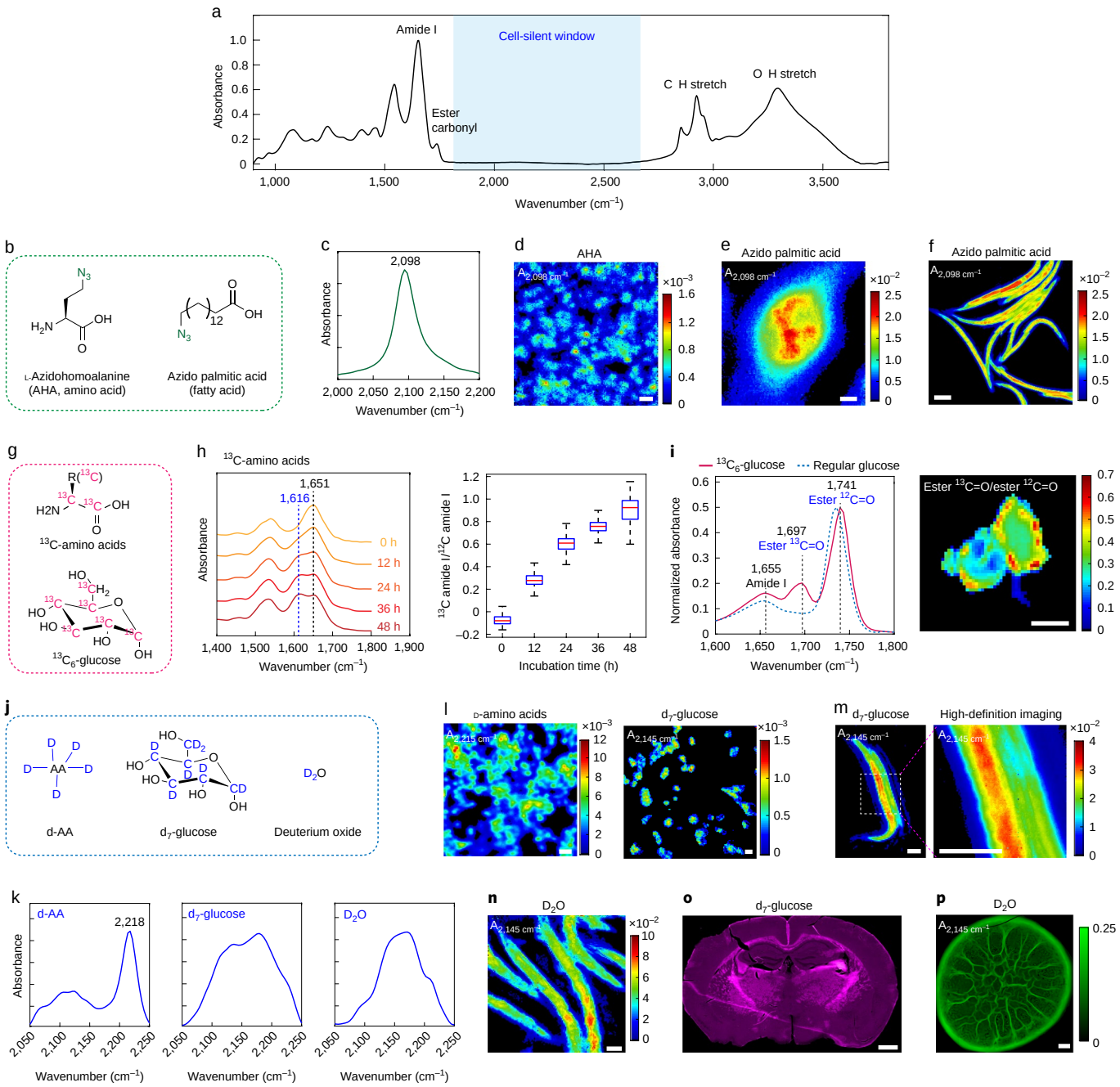

Fig. 1 | Design of MIR probes for metabolic imaging in cells, small organisms and mice. a, A typical IR absorption spectrum of biological samples. Cell-silent window, 1,800–2,700 cm^{-1}, where no peak exists from endogenous biomolecules. **b**, Metabolic precursors with azide probe. **c**, A single narrow azide peak in the cell-silent window. **d**, Imaging of newly synthesized protein in macrophage Raw264.7 cells with AHA. **e**, High-definition imaging of fatty acid uptake in a single Raw264.7 cell with azido-palmitic acid. **f**, Imaging of fatty acid incorporation into *C. elegans* with azido-palmitic acid. **g**, Precursors with ^{13}C substitution for forming metabolism-induced ^{13}C-carbonyl probe. **h**, Visualization on protein synthesis rate with ^{13}C-amino acids in MDA-MB-468 cells. The ratio of two peaks were analyzed among pixels (right). **i**, Visualization of de novo lipogenesis in differentiated 3T3-L1 adipocytes with ^{13}C-glucose. A ^{13}C ester peak appears at 1,741 cm^{-1} when $^{13}C_6$-glucose was added. Lipogenesis rate can be calculated by the ratio map of ester ^{13}C=O over ester ^{12}C=O. **j**, Metabolic precursors with carbon-deuterium probe. **k**, Spectral characterization of incorporated CD probes. Deuterated amino acids (d-AA) were imaged inside mammalian cells. d_7-glucose and D_2O were acquired by anabolic activity of *E. coli* bacteria. **l**, Imaging of d-AA and d_7-glucose in MDA-MB-468 cells. **m**, High-definition imaging of d_7-glucose anabolic activity in *C. elegans*. **n**, Imaging of D_2O-derived biosynthesis in *C. elegans*. **o**, Imaging glucose anabolic activity in whole brain with d_7-glucose. The image was generated by integrating the C–D band as 2,060–2,220 cm^{-1}. **p**, Imaging metabolic activity of a 4-d-old *P. aeruginosa* colony biofilm labeled with D_2O and imaged with a 4× objective (20.2-μm pixel size). Scale bars, 40 μm in **d**,**i**,**l**-**n**; 10 μm in **e**; 100 μm in **f** and 1 mm in **o**,**p**.

acid as two examples (Fig. 1b). By incubating the azide probe with cells, a single peak emerges at 2,098 cm^{-1} (Fig. 1c and Extended Data Fig. 1a,b). The cellular distribution of newly synthesized proteome can be visualized by using a single type of amino acid with AHA (Fig. 1d). High-definition imaging can also be achieved for azido-palmitic acid with a ~3-μm diffraction-limited resolution.

(Fig. 1e and Extended Data Fig. 1c). At the whole-organism level, active incorporation of the azido-palmitic acid into lipids in *Caenorhabditits elegans* can also be visualized (Fig. 1f and Extended Data Fig. 1d).

There are two design considerations behind a ^{13}C-edited carbonyl bond. First, the carbonyl bond is arguably the strongest IR mode in biomolecules. Indeed, amide I and ester carbonyl exhibit high ε around 800 and 290 $M^{-1}cm^{-1}$, respectively[29]. Second, carbonyl bonds in newly synthesized biomolecules can be shifted away from endogenous components by 30–40 cm^{-1} if ^{13}C-substituted essential metabolites are administered[30], thereby reporting metabolic activities. Here we employ ^{13}C-amino acids (^{13}C-AA) and ^{13}C-glucose as two metabolism-mediated vibrational probes (Fig. 1g). We first characterized the spectral shift in bacteria when $^{13}C_6$-glucose was supplied as the only carbon source. As expected, the amide I band redshifted to 1,616 from 1,651 cm^{-1} and the lipid ester band redshifted to 1,693 from 1,736 cm^{-1} (Extended Data Fig. 2a). When ^{13}C-AA is supplied to cultured mammalian cells, the original ^{12}C amide drops whereas the new ^{13}C amide peak rises with incubation time, with their ratio reflecting the protein turnover rate (Fig. 1h and Extended Data Fig. 2b). Moreover, we imaged glucose-derived de novo lipogenesis in 3T3-L1 differentiated adipocytes by monitoring the redshift of the ester carbonyl band during anabolism of ^{13}C-glucose (Fig. 1i and Extended Data Fig. 2c,d).

While the IR ε is relatively low (~10 $M^{-1}cm^{-1}$) for C–D bonds[18], deuterium-labeled probes are effective for economical delivery and labeling for animal experiments. Recent SRS work has reported exciting animal physiology applications by using heavy water (D_2O) and d_7-glucose[15,16]. We realize that these Raman probes also possess IR activity. For MIR metabolic imaging, we measured the FTIR spectra of incorporated C–D bonds from metabolic precursors including deuterated amino acids (d-AA), d_7-glucose and D_2O (Fig. 1j,k). With these deuterium-labeled probes, FTIR imaging is capable of tracking in situ metabolic activities with subcellular resolution in cells and multicellular organisms (Fig. 1l–n and Extended Data Fig. 2e). Metabolism of complex samples can be investigated. For example, by administrating d_7-glucose to the drinking water for lactating mice, glucose anabolism can be detected with FTIR in the brains of mice pups during embryonic and postnatal development (Fig. 1o and Extended Data Fig. 2f). For another example, D_2O labeling allows for the quantification of global biosynthetic activity during *Pseudomonas aeruginosa* colony biofilm growth (Fig. 1p).

MIR microscopy as a complementary platform to Raman for high-information-throughput imaging

Raman microscopy is hindered by low-information throughput, because of either limited spectral coverage or slow imaging speed (Fig. 2a). Spontaneous Raman captures broadband spectral information but suffers from an intrinsically slow imaging speed. SRS microscopy boosts the image acquisition speed via stimulated vibrational excitation by 1,000-fold[31]. As a trade-off, however, the spectral coverage is relatively narrow even with hyperspectral acquisition[12]. Moreover, as a nonlinear process, SRS requires tight laser focusing and point scanning, which is generally slow for large-area imaging. In comparison, MIR imaging can offer substantially higher information throughput (Fig. 2a), thanks to 10^{10} times larger IR absorption cross sections and an FPA-enabled widefield detection scheme. Similar to spontaneous Raman, FTIR microscopy is able to acquire a full vibrational spectrum but with faster speed. Analogs to SRS, high-power QCL allows selective excitation with a roughly 100–1,000 acceleration per frequency over FTIR[21,32].

It is helpful to experimentally benchmark the imaging speed (defined as area imaged per unit time) between broadband (that is, full spectral acquisition) FTIR and single-frequency SRS, especially in the context of metabolic imaging. D_2O-labeled mouse tissue is used as the common sample, as the C–D bond is both Raman and IR active. After adjusting imaging parameters of two techniques to achieve a similar signal-to-noise ratio from the same tissue region, broadband FTIR with a roughly 3.3 μm pixel size offers a comparable imaging speed to single-frequency SRS of a roughly 1 μm pixel size (Extended Data Fig. 3). This comparison is based on standard instruments, and more discussions on high-speed versions can be found in the literature[12,33]. Briefly, while the spatial resolution of SRS is expectedly finer, FTIR could be more advantageous to accommodate the full spectral coverage in a single scan (Fig. 2a).

Technical demonstration of multiplexed FTIR metabolic imaging with vibrational probes. Leveraging the full spectral coverage of FTIR, we demonstrate multiplexed metabolic imaging with dynamic information. It is important that the three categories of vibrational probes that we have introduced can be spectrally captured by FTIR simultaneously. As a proof-of-concept demonstration, we achieved three-color imaging on protein, lipid and carbohydrate metabolism. By culturing the differentiated adipocytes with a medium containing ^{13}C-AA, azido-palmitic acid and d_7-glucose, nascent protein synthesis, lipid scavenging and glucose anabolism can be monitored all at once at 1,616, 2,100 and 2,180 cm^{-1} (Fig. 2b). Compared to pre-adipocytes, differentiated adipocytes are highly active both in glucose-derived de novo lipogenesis and in lipid scavenging through azido-palmitic acid. For protein synthesis, an opposite trend in pre-adipocytes than adipocytes was observed based on the ratio map of ^{13}C amide/^{12}C amide (Fig. 2b). Our results collectively suggest adipocytes are metabolically specialized cells that use large amounts of glucose and fatty acids rather than amino acids for biomass production[34].

Multiplexed imaging on macromolecule biosynthesis in mice can be accomplished with D_2O probing. D_2O is a universal metabolic probe participating in synthesis of a variety of C–D bond containing macromolecules. By feeding mice with 25% D_2O in drinking water (a tested safe level[35,36]), we can monitor C–D signal accumulation in different organs. Figure 2c presents the FTIR spectrum and images from the cerebellum tissue of D_2O-labeled mice. A broad peak appears around 2,140 cm^{-1}, together with a shoulder peak at 2,175 cm^{-1} with distinct image patterns. We reasoned the two peaks are from different macromolecules. To verify the chemical origin, we digested the protein with proteinase K or dissolved lipids with methanol, and then acquired the spectra of the resulting tissues and compared to solution standard (Extended Data Fig. 4a). Consequently, the 2,140 and 2,175 cm^{-1} peaks are attributed to lipids and protein, respectively, in agreement with Raman characterization (Fig. 2d). A linear unmixing algorithm (Extended Data Fig. 4b) was used to retrieve the D_2O-dereived protein synthesis signal (CD_P) and de novo lipid synthesis signal (CD_L). As a result, protein and lipid synthesis activities can be visualized in situ by ratio maps as CD_P/amide and CD_L/CH_L, respectively (Fig. 2e). Furthermore, we generated a tissue-atlas of macromolecule synthesis (Fig. 2f and Extended Data Fig. 5).

Technical demonstration of DFIR metabolic imaging with vibrational probes

The superb acquisition speed of DFIR originates from two aspects. First, the tunable QCL can collect images at single frequencies. Second, the unprecedented light intensity of QCL renders it compatible with larger-area bolometer detector. DFIR has been recently commercialized with four QCL modules covering the fingerprint region of 900–1,800 cm^{-1}. To detect our vibrational probes in the cell-silent window, modified laser modules ranging from 1,200–1,800 and 2,000–2,300 cm^{-1} were used with a ×4 objective (pixel size, 4.25 μm) optimized for the new spectral regions (Fig. 2g).

To showcase DFIR microscopy in the context of vibrational probes, we first demonstrate single-cell profiling of nascent protein synthesis by giving cells ^{13}C-AA. Single-cell segmentation can be

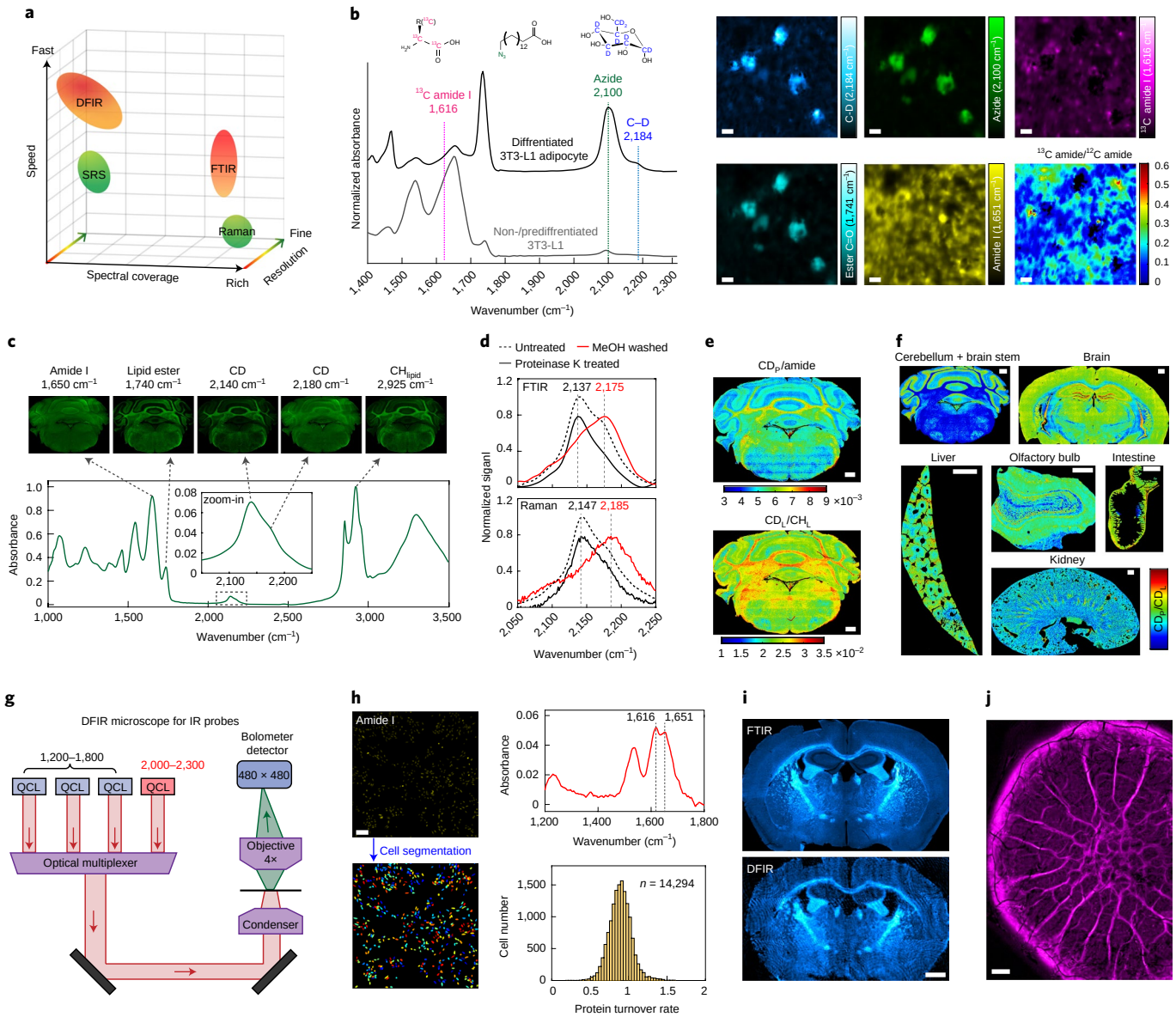

Fig. 2 | MIR metabolic imaging with high-information throughput. a, Comparison of MIR imaging techniques (FTIR and DFIR) with Raman imaging techniques (SRS and spontaneous Raman) in terms of imaging speed, spectral coverage and spatial resolution. While MIR techniques have poorer resolutions than Raman, they generally exhibit faster imaging speed or broader spectral coverage. **b**, Three-color metabolic probe imaging in differentiated 3T3-L1 adipocytes with ^{13}C-amino acid (^{13}C-AA), azido-palmitic acid (azido-PA) and d_7-glucose. Spectral features of three probes are highlighted. **c**, Multiplexed imaging of macromolecules synthesis activity in cerebellum of D_2O-labeled mouse. **d**, IR absorption and Raman spectra of cerebellum tissue treated with methanol wash (D-labeled protein signal in red) and proteinase K digestion (D-labeled lipid signal in solid black). **e**, Protein and lipid synthesis rate can be visualized by CD_P/amide and CD_L/CH_L on cerebellum tissue. CD_P and CD_L are C–D band absorbance after spectral unmixing, amide is absorbance of amide I peak at 1,650 cm^{-1} and CH_L is absorbance of CH_2 peak at 2,924 cm^{-1}. **f**, FTIR coupled with D_2O labeling enables tracking of in vivo protein and lipid synthesis on varied organs (cerebellum, brain stem, brain, liver, olfactory bulb, intestine and kidney). **g**, DFIR microscope customized for excitation of vibrational probes. **h**, DFIR imaging with ^{13}C-AA for single-cell protein synthesis activity profiling. MD-MA-468 cells were cultured in ^{13}C-AA medium for 24 h. **i**, Comparison of the imaging CD probe in D_2O-labeled brain tissue with FTIR and DFIR. Image was generated as absorbance at 2,140 cm^{-1} with baseline corrected. **j**, DFIR imaging on D_2O-labeled biofilm. The signal was generated as absorbance at 2,150 cm^{-1} with baseline corrected. Scale bars, 40 μm in **b**; 500 μm in **e** and **f**; 200 μm in **h**; 1 mm in **i** and **j**.

readily achieved under such resolution (Fig. 2h). A new ^{13}C amide I peak appears at 1,616 cm^{-1} (Fig. 2h), in consistent with FTIR measurement (Fig. 1h). The protein turnover rate of 14,000 segmented cells can be analyzed by DFIR in 2–3 min (Fig. 2h, from 1,500–1,800 cm^{-1}), representing an unprecedented throughput for chemical analysis of single cells.

Fast metabolic imaging of large-area tissues is another use for DFIR microscopy. We compared the DFIR imaging result with the FTIR on probing D_2O-labeled mouse brain tissue. The image pattern from DFIR matches well with the FTIR result (Fig. 2i). Regarding acquisition speed, it only takes DFIR less than 10 s to image the whole brain tissue with an area of 6 × 10-mm^2 at a single frequency and about 3 min for the 2,000–2,300 cm^{-1} range, which will require ~50 min for broadband FTIR (eight co-scans of signal). This imaging speed enables efficient large-scale imaging as demonstrated by mapping the heterogeneous CD pattern from D_2O-labeled *P. aeruginosa*

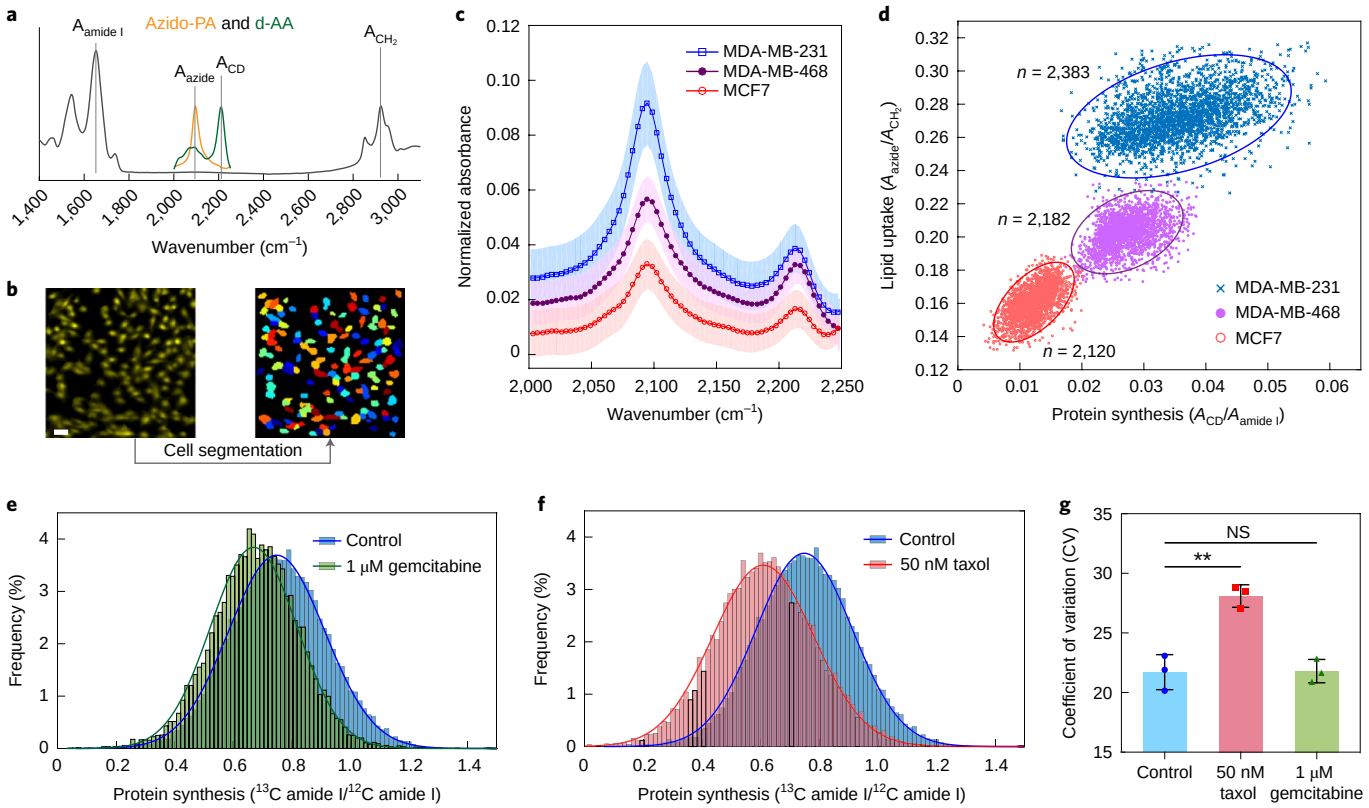

Fig. 3 | Single-cell metabolic profiling with FTIR and DFIR imaging. a, Spectrum for azido-PA and d-AA probes, allowing simultaneous two-color profiling. **b**, Example of single-cell segmentation for FTIR imaging with pixel size of 3.3 μm. Scale bar, 40 μm. **c**, Single-cell FTIR spectra on the probe region (normalize to amide I intensity) for three subtypes of human breast cancer cell. Shaded area indicates the s.d. of FTIR spectrum from different single cells (n = 45 cells for each subtype). **d**, Two-dimensional scatter plot on single-cell metabolic activity of three cell subtypes. The x axis is the protein synthesis rate calculated as $A_{CD}/A_{amide\ I}$ and the y axis is the lipid uptake rate calculated as A_{azide}/A_{CH_2}. Each dot represents single-cell information. Cells were cultured in CD-DMEM medium with 100 μM azido-PA for 24 h. Solid lines are error ellipses with 99% confidence. Cell number for MCF-7 is 2,120, for MDA-MB-468 is 2,182 and MDA-MB-231 is 2,383. **e**,**f**, Histogram of protein synthesis rate (calculated as ^{13}C amide I/^{12}C amide I) for MDA-MB-231 cells, collected by DFIR imaging, labeled with ^{13}C-AA for 24 h under conditions of no treatment and 1 μM gemcitabine for 24 h (**e**) and no treatment and 50 nM Taxol for 24 h (**f**). The solid curves were fitted with normal distribution. For control, $\mu = 0.748$, $\sigma = 0.164$; for gemcitabine, $\mu = 0.670$, $\sigma = 0.148$ and for Taxol, $\mu = 0.609$, $\sigma = 0.173$. **g**, CV values (means ± s.d., n = 3 cell cultures) of the single-cell protein synthesis rate distributions under control, 50-nM Taxol 24 h and 1-μM of gemcitabine 24 h. Heterogeneity was elevated under 50 nM Taxol 24 h (**P = 0.0054) but not changed under 1 μM gemcitabine 24 h (not significant (NS); P = 0.9359). P values were calculated from a two-tailed Welch's t-test. Cell numbers for each control group are 4,651, 7,756 and 6,671; for Taxol treatment 3,023, 6,195 and 6,018 and for gemcitabine treatment 3,414, 4,146 and 4,483.

biofilms (Fig. 2j). We note the DFIR images have some speckle patterns under the widefield configuration. This can be potentially mitigated by spatial noise dephasing[21,37] or point scanning system[33,38].

Application of single-cell metabolic profiling

Single-cell analysis can visualize hidden information beyond a population average. We showcase the applications of our technique in single-cell metabolic profiling. MIR microscopy has an intrinsic advantage in single-cell quantification, as it can readily yield single-cell spectra by integrating the entire cell volume naturally in the transmission mode at a suitable cell-level resolution. Besides, vibrational probes reveal valuable metabolic information. Moreover, its high-throughput capability is imperative for unveiling cellular heterogeneity that intrinsically requires analysis on a large cell population.

We demonstrate cell subtyping by probing metabolism. Breast cancer has multiple subtypes primarily classified by three receptors as estrogen receptor (ER), progesterone receptor (PR) and human epithelial growth receptor 2 (HER2). Three different breast cancer cell lines as MCF-7 (ER^+, PR^+, $HER2^-$), MDA-MB-468 (ER^-, PR^-, $HER2^-$) and MDA-MB-231 (ER^-, PR^-, $HER2^-$) were cultured with a medium containing d-AA and 100 μM azido-palmitic acid (Fig. 3a). After cell segmentation (Fig. 3b), single-cell spectra were generated by summing up all pixels inside (Fig. 3c). A two-dimensional scatter plot based on the lipid uptake and protein synthesis of individual cells present three clearly separable clusters (Fig. 3d), indicating distinct metabolic profiles between these three cell subtypes. The revealed order of metabolic activities agrees with the characterized aggressiveness: MCF-7 is noninvasive, MDA-MB-468 is metastatic and MDA-MB-231 is highly metastatic[39]. Moreover, the most aggressive MDA-MB-231 appears most heterogeneous (that is, wider spread of the cluster) especially on the protein synthesis rate (Fig. 3d).

We then harness high-speed DFIR to characterize metabolic heterogeneity during chemotherapeutic drug treatment (Taxol, a microtubule inhibitor, and gemcitabine, a deoxycytidine analog). We have shown that DFIR can collect selective spectrum over 10,000 cells in several minutes (Fig. 2h). For this drug study, MDA-MB-231 cells were exposed to Taxol or gemcitabine together with ^{13}C-AA labeling for 24 h. Low drug concentrations were used to assure cell viability. As expected, the protein synthesis activity was inhibited under both drug treatments (Fig. 3e,f). Additionally, the cellular metabolic heterogeneity can be evaluated by the coefficient of variation (CV, the ratio between standard deviation to the mean)

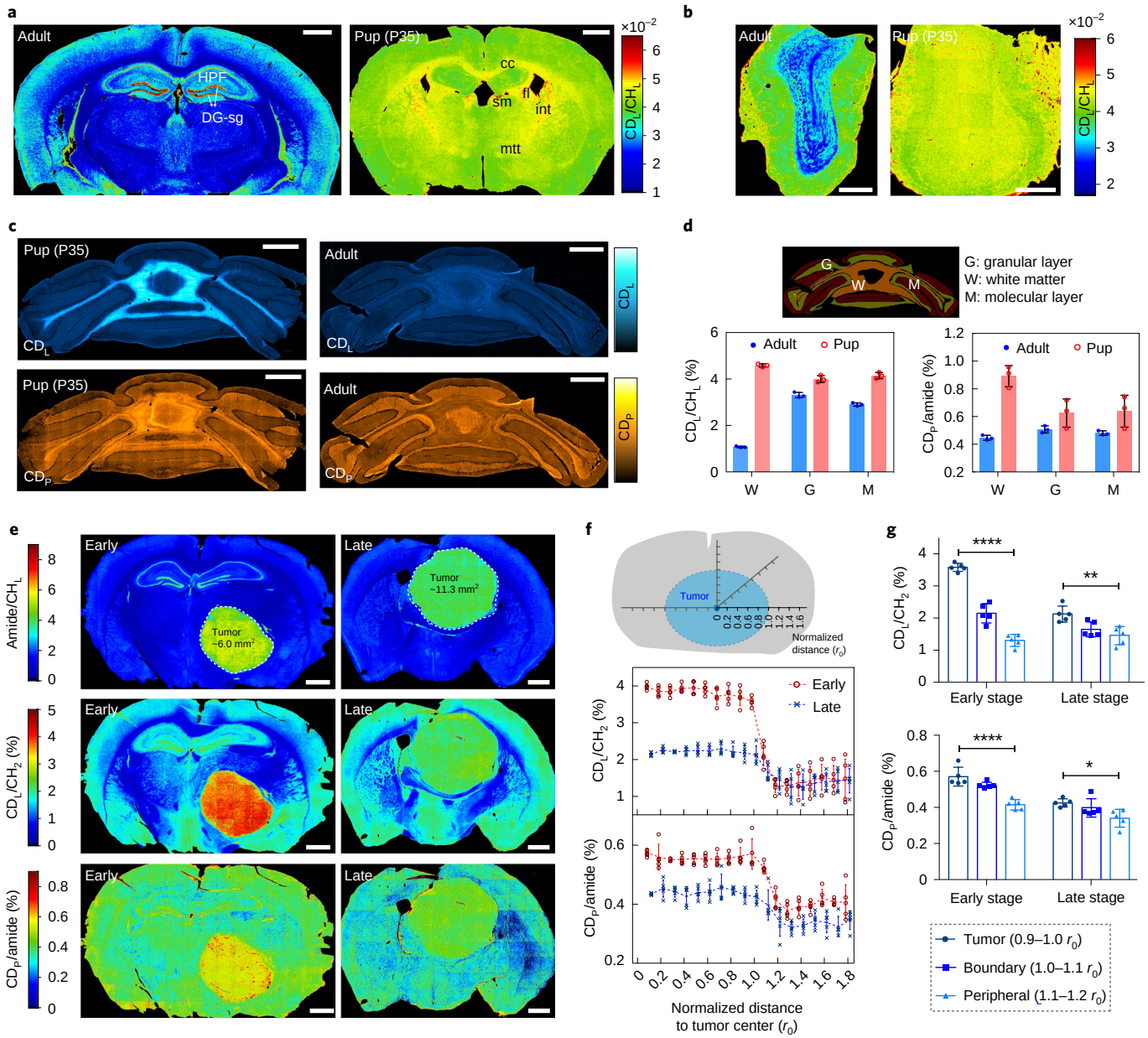

Fig. 4 | Application of MIR metabolic imaging on brain development and tumor progression. a–c, FTIR imaging of metabolic activity in mouse brain (**a**), olfactory bulb (**b**) and cerebellum (**c**) from P35 (35 d postnatal, 25% D_2O in drinking water for P1-P35) and adults (~4 months old, 25% D_2O in drinking water labeled for 35 d). **a**, the juvenile's brain has higher protein and lipid activities compared with the adult mouse especially in corpus callosum (cc), fimbria (fi), stria medullaris (sm), internal capsule (int) and mammilothalmic tract (mtt). **d**, Means ± s.d. of lipid (CD_L/CH_L) and protein (CD_P/amide) synthesis activity at different regions of cerebellum (n = 3 tissue samples). **e**, FTIR imaging of lipid and protein synthesis at two stages of glioblastoma tumor progression. Left column is the early stage and right column is the late stage. Margins of the tumors are marked in the first row with calculated solid tumor area size inside. **f**, Means ± s.d. of lipid (CD_L/CH_L) and protein (CD_P/amide) synthesis activity with the normalized distance to the tumor center (n = 5 selected directions). CD_L/CH_L and CD_P/amide at each distance r were averaged among ($r - 0.1\ r_0$) to r region. r_0 is the radius of solid tumor along this direction. **g**, Test on lipid and protein synthesis rate at the tumor region (0.9–1.0 r_0), boundary region (1.0–1.1 r_0) and peripheral brain region (1.1–1.2 r_0). One-way analysis of variance, CD_L/CH_L of the early stage: ****$P = 4.84 \times 10^{-9}$, $F = 140$; CD_L/CH_L of the late stage, **$P = 0.00373$, $F = 9.24$; CD_P/amide of the early stage, ****$P = 5.80 \times 10^{-5}$, $F = 24.5$ and CD_P/amide of the late stage, *$P = 0.0262$, $F = 5.01$. Scale bars, 1 mm.

(Fig. 3g). For instance, higher metabolic heterogeneity (larger CV) was observed under Taxol treatment. The high throughput of DFIR is essential to this finding of heterogeneity.

Application of metabolic imaging on brain development and tumor progression

Metabolic activities are tightly linked to regulation of brain development. We obtained FTIR images from different brain regions of juvenile and adult mice, which were administered with 25% D_2O in drinking water for the same duration. The full spectral coverage of FTIR allows us to calculate the ratio maps as CD_L/CH_L and CD_P/amide, which readily generate metabolic activities of the whole brain tissue (Fig. 4a–d and Extended Data Fig. 6). Regional alterations were found for the juvenile mouse compared with the adult mouse (Fig. 4a and Extended Data Fig. 6a,b). The granule cell layer of dentate gyrus (DG-sg) of hippocampus (HPF), a main neurogenic

area of adult brain, has substantially elevated lipid synthesis in adult mouse (Fig. 4a and Extended Data Fig. 6b). This finding is consistent with previous report that lipogenesis plays a critical role for proliferating neural stem and progenitor cells participating in adult neurogenesis[40]. Moreover, multi-layer structure from the surface to the center of olfactory bulb can be visualized by lipid channels (Fig. 4b and Extended Data Fig. 6c,d).

Myelination is an important developmental process whose timing is tightly regulated[41]. As an optimal model to study myelination, cerebellum has orderly and relatively simple architecture. A great difference can be readily observed by comparing the CD_P and CD_L between juvenile and adult mouse (Fig. 4c): high synthesis activity during myelination development in juvenile mouse cerebellum while little turnover in adult mouse. In contrast, the distributions of label-free channels are not much different (Extended Data Fig. 6e). Zooming into different regions inside cerebellum, myelination is not only restricted on the thick fibers but also expanded to the granular and even molecular layer on the parallel fibers during this P1-P35 window (Fig. 4d and Supplementary Fig. 1). This agrees with the literature that smallest axons become myelinated after P20 (ref. [41]). Protein synthesis is also more active during myelination especially in white matter, which may due to the required local synthesis of specialized protein such as myelin basic protein (Fig. 4d and Extended Data Fig. 6f,g).

Tumor progression and metastasis is a principal cause of cancer mortality. Glioblastoma multiforme (GBM) is one of the most aggressive tumors with unparalleled infiltration capability into normal brain tissue. The tumor margin of GBM has been visualized by label-free vibrational imaging based on the lipid and protein compositional difference between tumor and normal cells[42]. Rather than measuring the static chemical compositions, we reason the anabolic activity could be a unique marker to visualize tumor progression. To probe different stages of tumor progression, 25% D_2O was given to the GBM-bearing mice for 15 d starting at different days postinjection of U-87 human glioma cells. The tumor core can be clearly identified by amide/CH_L (Fig. 4e and Extended Data Fig. 7). Lipid and protein synthesis rates are evaluated by the ratio images as CD_L/CH_L and CD_P/amide, respectively (Fig. 4e). Quantitatively, metabolic activity curves were plotted with normalized distance to the tumor center for different tumor stages (Fig. 4f). At the early stage, both lipid and protein turnover exhibited step-like decrease going from tumor center to normal brain tissues (Fig. 4f,g). As the size of tumor core increased, metabolic difference between tumor and peripheral tissue started to decrease, and the tumor margin became blurred (Fig. 4f,g). This observation is consistent with previous work suggesting that lipogenesis[43] and increased protein synthesis[44] occur during carcinogenesis.

Discussion

Label-free imaging has been the prevalent model of MIR microscopy. Albeit powerful, they offer limited information about metabolic dynamics of specific pathways. Here we introduced a set of small vibrational probes, enabling new functional capabilities to image metabolic activity in situ. Two high-information-throughput MIR platforms of FTIR and DFIR are demonstrated. Although the current resolution (~3 μm) is poorer than Raman-based techniques, MIR methods are superior in spectral coverage and imaging speed (Fig. 2). FTIR microscopes are commercially available and our DFIR is a custom-modified commercial system, rendering readily accessible to biologists. It should be straightforward to translate our probes to other high-resolution schemes such as MIR photothermal[45], MIR photoacoustic[46] and atomic force microscopy IR spectroscopy[47], enabling submicrometer- to nanoscale-metabolic imaging. Additionally, MIR imaging is also able to image live cells and small organisms[22,48]. New detection schemes such as photoacoustic[46,49] and field-resolved IR spectroscopy[50], which are noninvasive and water-background free, could be promising for in vivo applications in large animals.

Probe-wise, azide bond, ^{13}C-edited carbonyl bond and ^{2}H-labeled probes are complementary with different uses (Fig. 1). First, spectrally resolvable probes allow multiplexed metabolic imaging. Second, multifaceted functional purposes can be probed. For example, while an azide probe allows for the tracking of the metabolism of a specific metabolite (including methionine and palmitic acid demonstrated here, as well as many other targets such as chemical drugs), the ^{13}C-carbonyl bond of amide I and ester carbonyl derived from ^{13}C-AA and ^{13}C-glucose can map global proteome and lipid synthesis activities. For another example, d_7-glucose and ^{13}C-glucose track hydrogen flow and carbon flow of glucose metabolism, respectively. Third, for metabolism-mediated probes (such as ^{13}C-AA, ^{13}C-glucose and D_2O), the targeted IR modes only appear after metabolism of labeled precursors, which is meaningful in monitoring particular biosynthetic pathways. Fourth, the in vivo delivery and bio-distribution are different for different probes. For instance, although the resulting MIR signal is less pronounced than azide or carbonyl bonds in cultured cells, D_2O and d_7-glucose are particularly effective for studying animal physiology[15,16].

Application-wise, MIR-based metabolic imaging is uniquely suited for studies in which fast speed or rich spectral information is essential whereas submicrometer resolution is not necessary. This could open up a broad range of applications. For example, metabolic activity profiling could be performed at the single-cell level. The high-content, high-throughput capability is imperative to cell type classification and heterogeneity characterization (Fig. 3). In addition, tissue-level metabolic imaging can be carried out on a large area that is compatible to the whole organ level (Fig. 4), which can facilitate comprehensive and holistic biological understanding.

Online content

Any methods, additional references, Nature Research reporting summaries, source data, extended data, supplementary information, acknowledgements, peer review information; details of author contributions and competing interests; and statements of data and code availability are available at https://doi.org/10.1038/s41592-020-0883-z.

Received: 15 January 2020; Accepted: 27 May 2020;
Published online: 29 June 2020

References

1. Kandel, E. R. The molecular biology of memory storage: a dialogue between genes and synapses. *Science* **294**, 1030 (2001).
2. Roche, F. K., Marsick, B. M. & Letourneau, P. C. Protein synthesis in distal axons is not required for growth cone responses to guidance cues. *J. Neurosci.* **29**, 638 (2009).
3. Hinz, F. I., Dieterich, D. C., Tirrell, D. A. & Schuman, E. M. Noncanonical amino acid labeling in vivo to visualize and affinity purify newly synthesized proteins in larval zebrafish. *ACS Chem. Neurosci.* **3**, 40–49 (2012).
4. Zilberter, Y. & Zilberter, M. The vicious circle of hypometabolism in neurodegenerative diseases: ways and mechanisms of metabolic correction. *J. Neurosci. Res.* **95**, 2217–2235 (2017).
5. Hebert, S. L. & Nair, K. S. Protein and energy metabolism in type 1 diabetes. *Clin. Nutr.* **29**, 13–17 (2010).
6. Pavlova, N. N. & Thompson, C. B. The emerging hallmarks of cancer metabolism. *Cell Metab.* **23**, 27–47 (2016).
7. Kim, M. M., Parolia, A., Dunphy, M. P. & Venneti, S. Non-invasive metabolic imaging of brain tumours in the era of precision medicine. *Nat. Rev. Clin. Oncol.* **13**, 725–739 (2016).
8. Steinhauser, M. L. et al. Multi-isotope imaging mass spectrometry quantifies stem cell division and metabolism. *Nature* **481**, 516–519 (2012).
9. Palonpon, A. F., Sodeoka, M. & Fujita, K. Molecular imaging of live cells by Raman microscopy. *Curr. Opin. Chem. Biol.* **17**, 708–715 (2013).
10. Wei, L. et al. Live-cell bioorthogonal chemical imaging: stimulated Raman scattering microscopy of vibrational probes. *Acc. Chem. Res.* **49**, 1494–1502 (2016).

11. Shen, Y., Hu, F. & Min, W. Raman imaging of small biomolecules. *Annu. Rev. Biophysics.* **48**, 347–369 (2019).
12. Hu, F., Shi, L. & Min, W. Biological imaging of chemical bonds by stimulated Raman scattering microscopy. *Nat. Methods* **16**, 830–842 (2019).
13. Lee, H. J. et al. Assessing cholesterol storage in live cells and *C. elegans* by stimulated Raman scattering imaging of phenyl-diyne cholesterol. *Sci. Rep.* **5**, 7930 (2015).
14. Schiessl, K. T. et al. Phenazine production promotes antibiotic tolerance and metabolic heterogeneity in *Pseudomonas aeruginosa* biofilms. *Nat. Commun.* **10**, 762 (2019).
15. Shi, L. et al. Optical imaging of metabolic dynamics in animals. *Nat. Commun.* **9**, 2995 (2018).
16. Zhang, L. et al. Spectral tracing of deuterium for imaging glucose metabolism. *Nat. Biomed. Eng.* **3**, 402–413 (2019).
17. Lin-Vien, D., Colthup, N. B., Fateley, W. G. & Grasselli, J. G. *The Handbook of Infrared and Raman Characteristic Frequencies of Organic Molecules* (Academic Press, 1991).
18. Ma, J., Pazos, I. M., Zhang, W., Culik, R. M. & Gai, F. Site-specific infrared probes of proteins. *Annu. Rev. Phys. Chem.* **66**, 357–377 (2015).
19. Suydam, I. T. & Boxer, S. G. Vibrational Stark effects calibrate the sensitivity of vibrational probes for electric fields in proteins. *Biochemistry* **42**, 12050–12055 (2003).
20. Pilling, M. & Gardner, P. Fundamental developments in infrared spectroscopic imaging for biomedical applications. *Chem. Soc. Rev.* **45**, 1935–1957 (2016).
21. Yeh, K., Kenkel, S., Liu, J.-N. & Bhargava, R. Fast infrared chemical imaging with a quantum cascade laser. *Anal. Chem.* **87**, 485–493 (2015).
22. Haase, K., Kröger-Lui, N., Pucci, A., Schönhals, A. & Petrich, W. Real-time mid-infrared imaging of living microorganisms. *J. Biophotonics.* **9**, 61–66 (2016).
23. Gazi, E. et al. A FTIR microspectroscopic study of the uptake and metabolism of isotopically labelled fatty acids by metastatic prostate cancer. *Vib. Spectrosc.* **50**, 99–105 (2009).
24. Bai, Y., Zhang, D., Li, C., Liu, C. & Cheng, J.-X. Bond-selective imaging of cells by mid-infrared photothermal microscopy in high wavenumber region. *J. Phys. Chem. B.* **121**, 10249–10255 (2017).
25. Clède, S. et al. Synchrotron radiation FTIR detection of a metal-carbonyl tamoxifen analog. Correlation with luminescence microscopy to study its subcellular distribution. *Biotechnol. Adv.* **31**, 393–395 (2013).
26. McCoy, S. & Caughey, W. S. Infrared studies of azido, cyano, and other derivatives of metmyoglobin, methemoglobin, and hemins. *Biochemistry* **9**, 2387–2393 (1970).
27. Błasiak, B., Londergan, C. H., Webb, L. J. & Cho, M. Vibrational probes: from small molecule solvatochromism theory and experiments to applications in complex systems. *Acc. Chem. Res.* **50**, 968–976 (2017).
28. Prescher, J. A. & Bertozzi, C. R. Chemistry in living systems. *Nat. Chem. Biol.* **1**, 13–21 (2005).
29. Pazos, I. M., Ghosh, A., Tucker, M. J. & Gai, F. Ester carbonyl vibration as a sensitive probe of protein local electric field. *Angew. Chem. Int. Ed.* **53**, 6080–6084 (2014).
30. Muhamadali, H., Chisanga, M., Subaihi, A. & Goodacre, R. Combining Raman and FT-IR spectroscopy with quantitative isotopic labeling for differentiation of E. coli cells at community and single cell levels. *Anal. Chem.* **87**, 4578–4586 (2015).
31. Cheng, J.-X. & Xie, X. S. Vibrational spectroscopic imaging of living systems: an emerging platform for biology and medicine. *Science* **350**, aaa8870 (2015).
32. Wrobel, T. P. & Bhargava, R. Infrared spectroscopic imaging advances as an analytical technology for biomedical sciences. *Anal. Chem.* **90**, 1444–1463 (2018).
33. Yeh, K., Lee, D. & Bhargava, R. Multicolor discrete frequency infrared spectroscopic imaging. *Anal. Chem.* **91**, 2177–2185 (2019).
34. Hosios, AaronM. et al. Amino acids rather than glucose account for the majority of cell mass in proliferating mammalian cells. *Dev. Cell.* **36**, 540–549 (2016).
35. Peng, S. K., Ho, K. J. & Taylor, C. B. Biologic effects of prolonged exposure to deuterium oxide. A behavioral, metabolic, and morphologic study. *Arch. Pathol.* **94**, 81–89 (1972).
36. Hodel, A., Gebbers, J. O., Cottier, H. & Laissue, J. A. Effects of prolonged moderate body deuteration on proliferative activity in major cell renewal systems in mice. *Life Sci.* **30**, 1987–1996 (1982).
37. Ran, S., Berisha, S., Mankar, R., Shih, W.-C. & Mayerich, D. Mitigating fringing in discrete frequency infrared imaging using time-delayed integration. *Biomed. Opt. Express* **9**, 832–843 (2018).
38. Mittal, S. et al. Simultaneous cancer and tumor microenvironment subtyping using confocal infrared microscopy for all-digital molecular histopathology. *Proc. Natl Acad. Sci. USA* **115**, E5651 (2018).
39. Liu, Y.-L. et al. Assessing metastatic potential of breast cancer cells based on EGFR dynamics. *Sci. Rep.* **9**, 3395 (2019).
40. Knobloch, M. et al. Metabolic control of adult neural stem cell activity by Fasn-dependent lipogenesis. *Nature* **493**, 226–230 (2013).
41. Snaidero, N. & Simons, M. Myelination at a glance. *J. Cell Sci.* **127**, 2999 (2014).
42. Ji, M. et al. Rapid, label-free detection of brain tumors with stimulated Raman scattering microscopy. *Sci. Transl. Med.* **5**, 201ra119 (2013).
43. Röhrig, F. & Schulze, A. The multifaceted roles of fatty acid synthesis in cancer. *Nat. Rev. Cancer* **16**, 732–749 (2016).
44. Clemens, M. J. Targets and mechanisms for the regulation of translation in malignant transformation. *Oncogene* **23**, 3180–3188 (2004).
45. Zhang, D. et al. Depth-resolved mid-infrared photothermal imaging of living cells and organisms with submicrometer spatial resolution. *Sci. Adv.* **2**, e1600521 (2016).
46. Shi, J. et al. High-resolution, high-contrast mid-infrared imaging of fresh biological samples with ultraviolet-localized photoacoustic microscopy. *Nat. Photonics* **13**, 609–615 (2019).
47. Dazzi, A. & Prater, C. B. AFM-IR: technology and applications in nanoscale infrared spectroscopy and chemical imaging. *Chem. Rev.* **117**, 5146–5173 (2017).
48. Andrew Chan, K. L. & Kazarian, S. G. Attenuated total reflection Fourier-transform infrared (ATR-FTIR) imaging of tissues and live cells. *Chem. Soc. Rev.* **45**, 1850–1864 (2016).
49. Pleitez, M. A. et al. Label-free metabolic imaging by mid-infrared optoacoustic microscopy in living cells. *Nat. Biotechnol.* **38**, 293–296 (2020).
50. Pupeza, I. et al. Field-resolved infrared spectroscopy of biological systems. *Nature* **577**, 52–59 (2020).

Methods

Cell lines and materials. All cell lines were purchased from ATCC including HeLa (ATCC CCL-2), Raw264.7 (ATCC TIB-71), MDA-MB-231 (ATCC HTB-26), MDA-MB-468(ATCC HTB-132), MCF-7 (ATCC HTB-22), 3T3-L1 MBX (ATCC CRL-3242), U-87 MG (ATCC HTB-14). Azido-palmitic acid (1346) and L-AHA (1066) were purchased from Click chemistry tools. D-glucose (1,2,3,4,5,6,6-D7, 97-98%, DLM-2062), algal amino acid mixture (U-13C, 97-99%, CLM-1548), 2-deoxy-D-glucose (U-13C6, 99%, CLM-10466) were purchased from Cambridge isotope laboratories. Deuterium oxide (151882), Taxol (T7402) and Gemcitabine (G6423) were purchased from Sigma-Aldrich. DMEM medium (11965), FBS (10082), penicillin/streptomycin (1514), DMEM medium without L-methionine, L-cysteine and L-glutamine (21013), DMEM without glucose (11966) and proteinase K (EO0491) were purchased from ThermoFisher Scientific. CaF_2 substrates (CAFP25-1, CAFP13-1 and CAFP-76-26-1U) were purchased from Crystran.

FTIR and DFIR microscopy, image acquisition and data preprocessing. Agilent Cary 620 Imaging FTIR equipped with an Agilent 670-IR spectrometer and 128×128-pixels FPA HgCdTe (mercury cadmium telluride, MCT) detector was used in the transmission mode. A background spectrum was collected on a clean CaF_2 substrate using 128–256 scans at 8 cm^{-1} spectral resolution. Sample spectra were recorded using 64–128 scans for cells and 8–32 scans for tissues at 8 cm^{-1} spectral resolution. A ×25 IR objective (pixel size, 3.3 µm, 0.81 numerical aperture (NA)) and ×15 IR objective (pixel size, 5.5 µm, 0.62 NA) were used for cell and tissue imaging. A ×4 IR objective (pixel size, 20.2 µm) was used for *P. aeruginosa* biofilm imaging. High-definition FTIR imaging was collected at pixel size of 0.66 µm with a ×25 IR objective under high-magnification mode achieved through second magnification with intermediate optics. For probes around 2,100 cm^{-1}, the resolution can be estimated as $\frac{1}{2\nu NA} = \frac{1}{2{,}100\ cm^{-1} \times 2 \times 0.81} = 2.9\ \mu m$. Data preprocessing was carried out using commercial software Cytospec with following steps: (1) denoise the spectra with PCA noise reduction; (2) quality test based on full spectral integration and (3) rubber-band baseline correction or polynomial baseline correction was applied for spectral correction.

For DFIR imaging, a custom-modified Spero-QT microscope (Daylight Solutions, Inc.) is equipped with four QCL modules with spectral coverage from 1,200–1,800 and 2,000–2,300 cm^{-1}. The microscope is constantly purged with dry nitrogen and a plastic box was implemented to cover the sample compartment. A ×4 IR objective (pixel size, 4.25 µm, 0.3 NA) and a non-N_2-liquid cooled microbolometer FPA with 480×480 pixels were applied for all data collection on the transmission mode. For spectral sweeping, data was collected with 4 cm^{-1} spectral resolution. As for data preprocessing, cell spectra were corrected by subtracting the off-resonance signal as the absorbance at 1,800 cm^{-1}. For tissue imaging with D_2O probing, a linear baseline correction was applied for the 2,000–2,300 cm^{-1} region. The fringe patterns from the coherent QCL source were further de-noised by minimum noise fraction transform with stripe noise pattern using commercial software Epina ImageLab.

SRS microscopy. Synchronized pump (tunable from 720–990 nm) and Stokes (fixed at 1,064.2 nm) beams with both 6-ps pulse width and 80-MHz repetition rate are provided by a picoEmerald system from Applied Physics & Electronic, Inc. The intensity of the 1,064 nm Stokes beam was modulated sinusoidally by a built-in electro-optic modulator at 8 MHz with a modulation depth of more than 95%. Spatially and temporally-overlapped pump and Stokes beams were coupled into an inverted laser-scanning microscope (FV1200MPE, Olympus). A ×25 water objective (XLPlan N, 1.05 NA, MP, Olympus) was used. The forward-going pump and Stokes beams after passing through the samples were collected in transmission with a condenser (oil immersion, 1.4 NA, Olympus). A large-area (10×10 mm) Si photodiode (FDS1010, Thorlabs) was used for pump intensity detection after filtering the Stokes beam completely with two high-optical-density bandpass filter (890/220 CARS, Chroma Technology). The output current of the photodiode was then sent to a fast lock-in amplifier (HF2LI, Zurich Instruments) for signal demodulation.

Probe preparation and media recipe for cell labeling. *Palmitic acid-bovine serum albumin (BSA) solution.* For the solution, couple azido-palmitic acid with BSA to prepare a 2-mM stock solution. Prepare 20 mM sodium palmitic acid solution by dissolving palmitic acid in NaOH solution with the following recipe: azido-PA (5.5 mg) + 1.0 ml dd-H_2O + 35 µl 1 M NaOH. Mix and incubate the solution in 70 °C water baths until no oil droplets are visible. Then slowly add the sodium palmitic acid solution into 2.7 ml 20% BSA under room temperature water baths. Quickly add 6.3 ml DMEM culture medium and filter the solution with a 0.22-µm sterile filter.

AHA labeling medium. DMEM medium without L-methionine, L-cysteine and L-glutamine (Invitrogen, 21013) was supplemented with 5 mM AHA, 0.2 mM L-cystine, 4 mM L-glutamine, 10% FBS (10082, Invitrogen) and 1% penicillin/streptomycin (15140, Invitrogen).

^{13}C-AA DMEM. For this, 4 mg ml^{-1} algae ^{13}C-amino acids mix (CLM-1548, Cambridge isotope) was dissolved in dd-H_2O with 10% FBS and 1% penicillin/streptomycin. Other components (vitamin, inorganic salts and glucose) are exactly the same as the normal DMEM medium (11965, Invitrogen).

Deuterated amino acids medium (CD-DMEM). This medium was prepared in the same way to the D-AA medium for HeLa cells as previously described[51].

d_7-glucose and $^{13}C_6$-glucose labeling medium. DMEM without glucose (11966, Invitrogen) was supplemented with 4.5 mg ml^{-1} d_7-glucose or $^{13}C_6$-glucose, 10% FBS and 1% penicillin/streptomycin.

For cell labeling experiments, cells were first seeded onto clean CaF_2 substrates and cultured with their usual culture media for 24 h. To introduce the IR probes, replace the culture media with required labeling media for described labeling time. Cells were then fixed with 4% formaldehyde (PFA) for 20 min, washed three times with HBSS buffer and three times with dd-H_2O (ref. [52]). The samples were air-dried under room temperature before imaging.

3T3-L1 differentiation. Low passage of 3T3-L1 MBX fibroblasts (early than passage 10) were seeded onto clean CaF_2 substrate (25-mm dia) in a six-well plate with a density of 3×10^4 cells per well in growth medium (DMEM (11965, Invitrogen) supplemented with 10% FBS (10082, Invitrogen) and 1× penicillin/streptomycin (15140, Invitrogen)) and were gown to confluence for 6 d, with changing growth medium every 2 d. Differentiation was induced by incubating the cells in differentiation medium (growth medium supplemented with 3.5 µg ml^{-1} bovine insulin (Sigma I0516), 500 µM methylisobutylxanthine (Sigma I5879) and 250 nM dexamethasone (Sigma D1756)) for 72 h. After 72 h, replace with maintenance medium (growth medium with 3.5 µg ml^{-1} bovine insulin) for 7 d, with medium replaced every 2 d, for full differentiation.

Three-color imaging on differentiated 3T3-L1 cells. Fully differentiated 3T3-L1 MBX adipocytes seeded on CaF_2 substrate were cultured in d_7-glucose substituted DMEM medium with 3.5 µg ml^{-1} bovine insulin for 48 h. The medium is then replaced with d_7-glucose and ^{13}C-AA DMEM containing 100-µM azido-palmitic acid for 24 h. Cells were then fixed with 4% PFA at room temperature for 20 min and washed three times with PBS buffer and three times with dd-H_2O. The samples were air dried before imaging.

***C. elegans* and *P. aeruginosa* biofilm labeling.** *C. elegans* wild-type (N2) was maintained at 20 °C using nematode growth media (NGM) and *E. coli* strain OP50 as a food source. For D_2O treatment, D_2O was added to replace 20% of the H_2O in nematode growth media plates. For d_7-glucose and azido-palmitic acids labeling, OP50 bacterial culture were mixed with the probes at indicated concentrations and then seeded onto usual nematode growth media plates. Then, 24 h later, eggs were placed onto these plates and grew until L4 stage. Worms were then collected, washed with M9 buffer and fixed with 4% PFA for 30 min and washed with M9 buffer. Those fixed worms were further washed with three times of dd-H_2O and subsequently placed onto CaF_2 substrate and air dried before imaging.

The agar medium of 2% tryptone (Teknova) and 2% agar (Teknova) was autoclaved and D_2O was added in a 1:1 ratio for final concentrations of 1% tryptone, 1% agar in 1:1 of D_2O:H_2O. Coomassie Blue (OmniPur, MilliporeSigma) and Congo Red (Alfa Aesar) were added to the agar medium to final concentrations of 20 and 40 µg ml^{-1}, respectively. The agar medium was poured in two layers of 3 ml (bottom layer) and 1 ml (top layer) into 35×10 mm^2 round Petri dishes (25373-041, VWR). Biofilms were prepared by spotting 5 µl of mid-exponential phase bacterial culture of *P. aeruginosa* UCBPP-PA14 (WT strain, stock no. LD0) on agar medium. Biofilms were incubated at 25 °C in the dark for 96 h. For FTIR imaging, the top layer of agar with the biofilm was moved onto CaF_2 substrate and air dried.

Mouse labeling and mouse tumor xenograft. The animal protocol for mice studies was approved by Columbia University Institutional Animal Care and Use Committee (IACUC) (AC-AABD1552). All experiments using mice were conducted in strict adherence to the ethical regulations of Columbia University IACUC. Wild-type ~3–4-month-old female adult C57BL/6J mice were purchased from the Jackson Laboratory.

To establish the glioblastoma xenograft model, intracranial implantation of U87MG human glioma cells were performed on nude mice (J:NU, Jackson Laboratory). The mice were anesthetized and stabilized in stereotaxic instrument (David Kopf Instruments), and then the head skin was cut open to make the skull bone exposed, a small section (2 mm in diameter) on the frontal region of the skull was ground with a dental drill (Braintree Scientific) until it became transparent and soft. 1.5×10^5 U87MG tumor cells in 3 µl were injected into the frontal region of the cerebral cortex over the course of 5 min using a 1.5-mm glass capillary (injection tip is a few hundred micrometers in diameter) via the grounded region. Mouse head skin was then closed with silk sutures (Harvard Apparatus) after implantation. Four mice were treated in this way with all four mice survived. Two mice were killed at 15 d post xenograft (early stage) and two mice were killed at 26 d post xenograft (late stage) for imaging. During tumor progression, the animals were monitored daily, including weekends, for any sign of morbidity, including weight loss, inability to eat or drink, dehydration, inability to maintain balance or

unresponsiveness to noxious external stimuli, such as tow-pinch withdrawal test. When these signs are apparent, the animal will be euthanized.

For D_2O probing experiments, 25% D_2O in drinking water was given to the mice for certain days. For glioblastoma bearing mice, 25% D_2O were provided for 15 d with different starting time points posttumor implantation (early stage, label from day 0–15 postxenograft; late stage, label from day 11–26 postxenograft), then killed for imaging experiments.

For the d_7-glucose probing experiment, 2% d_7-glucose was administered to the pregnant or the lactating female mouse in drinking water from E11 to P21. Mice were anesthetized with isoflurane and scarified by cervical dislocation and organs were then collected. The organs were fixed with 4% PFA for 2 d.

For tissue slicing, the organs were embedded in 6% agarose gel and sliced into 10–20 µm thin slices with a vibratome (Leica) in HBSS buffer. The collected tissue slices were washed twice with HBSS buffer and once with dd-H_2O. The samples were then mounted on CaF_2 substrates for air drying.

Spectral unmixing algorithms and single-cell analysis. Retrieval of CD_P and CD_L signals for D_2O labeled mouse. To measure the IR spectra for D-labeled protein and lipid, tissue slices (100 µm thick) from various organs were soaked in either pure methanol for 2 d at room temperature to dissolve lipids or in proteinase K solution (400 µg ml^{-1} proteinase K, 0.5 mM EDTA in 30 mM Tris buffer) on a 37 °C shaker to digest protein. The resolved spectral unmixing algorithm can be referred to Extended Data Fig. 4.

Retrieval of ^{12}C amide I and ^{13}C amide I. The unmixing coefficients were measured from spectra of bacteria growing in the media with $^{12}C_6$-glucose or $^{13}C_6$-glucose as the only carbon source (Extended Data Fig. 2a). The final linear combination algorithm was given as:

$$^{12}\text{C-amide} = 1.281 \times A_{1651} - 0.548 \times A_{1616}$$

$$^{12}\text{C-amide} = -0.657 \times A_{1651} + 1.281 \times A_{1616}$$

Retrieval of ^{12}C ester carbonyl and ^{13}C ester carbonyl. The cross-talk from the ^{12}C amide I peak to the ^{13}C ester carbonyl peak was calculated from spectra of bacteria growing in the media with $^{12}C_6$-glucose or $^{13}C_6$-glucose as the only carbon source (Extended Data Fig. 2a). The final linear combination algorithm was given as:

$$^{12}\text{C-carbonyl} = A_{1741}$$

$$^{13}\text{C-carbonyl} = A_{1697} - 0.31 \times A_{1651}$$

Unmixing in d-AA and azido-PA dual-probe experiment. The cross-talk from the broad C–D band to the narrow azide peak was calculated from spectra of single-probe labeling experiment. The final algorithm was given as:

$$\text{Azido-PA} = A_{2095}$$

$$\text{d-AA} = A_{2215} - 0.0216 \times A_{2095}$$

For single-cell analysis in Figs. 2h and 3, cell segmentation was first performed with an open-source software CellProfiler[53] based on the amide image for ^{13}C-AA labeling (data in Fig. 2h and Fig. 3e–g) and on the sum of azide image and C-D image for two-probe labeling (data in Fig. 3a–d). Single-cell spectra were generated by summing up all pixels inside after pixel-based spectral preprocessing. All metabolic rates (including C–D/amide I, azide/CH_2 and ^{13}C amide I/^{12}C amide I) were calculated based on single-cell spectra.

Statistics and reproducibility. Statistical analysis was carried out using MATLAB (R2016a) and GraphPad Prism 7. Data are presented as mean ± s.d. with statistical significance if required (not significant $P \geq 0.5$, $^*P < 0.05$, $^{**}P < 0.01$, $^{***}P < 0.001$, $^{****}P < 0.0001$ with the exact P values in the figure legends). P values were calculated using a two-tailed Welch's t-test in Fig. 3g. One-way analysis of variance was used to compare more than two groups of data in Fig. 4g. All values of n are provided in the figure legends. In box plot (Fig. 1h), center indicates the median, and the minima and maxima of the box indicate the 25th and 75th percentiles. The n for each time points from 0 to 48 h are 3,496, 5,304, 2,983, 4,964 and 7,721 pixels, respectively. Statistics source data for Figs. 3–4 are provided in Source Data. For Fig. 1, experiments in Fig. 1a,c–e,k were repeated five times independently with similar results; experiments in Fig. 1f,i,l–n,p were repeated three times independently with similar results; experiments in Fig. 1o were repeated on three tissue slices with similar results. For Fig. 2, experiments in b, d and j were repeated three times independently with similar results; experiments in Fig. 2c,e,f,i were repeated on three tissue slices for each organ with similar results. For Fig. 3, experiments in a and b were repeated five times independently with similar results; experiments in Fig. 3d were repeated on three cell cultures independently with similar results. For Fig. 4, experiments in a–c and e were repeated on three tissue slices, each with similar results.

Reporting Summary. Further information on research design is available in the Nature Research Reporting Summary linked to this article.

Data availability

The source data for Figs. 3 and 4 are available online as Source Data. Other data that support the findings of this study are available from the corresponding author upon reasonable request.

References

51. Wei, L. et al. Imaging complex protein metabolism in live organisms by stimulated Raman scattering microscopy with isotope labeling. *ACS Chem. Biol.* **10**, 901–908 (2015).
52. Baker, M. J. et al. Using Fourier transform IR spectroscopy to analyze biological materials. *Nat. Protoc.* **9**, 1771–1791 (2014).
53. Carpenter, A. E. et al. CellProfiler: image analysis software for identifying and quantifying cell phenotypes. *Genome Biol.* **7**, R100 (2006).

Acknowledgements

We thank K.A. McHose and L. Tisinger from Agilent Inc. for technical supports on FTIR microscope and Lu Wei for helpful discussion. W.M. acknowledges support from NIH R01 (GM128214 and GM128214-02S1) and R01 (EB029523). L.E.P.D. was supported by NIH/NIAID grant no. R01 AI103369.

Author contributions

Lixue Shi performed spectroscopy and microscopy studies and analyzed the data. X.L. performed single-cell study and data analysis. Lingyan Shi contributed to mice study and data analysis. H.T.S. and J.R. contributed to DFIR microscope custom design. L.J.K., C.R.E. and L.E.P.D. contributed to biofilm study. C.Z. contributed to *C. elegans* study. Lixue Shi and W.M. conceived the concept and wrote the manuscript with input from all authors.

Competing interests

The authors declare no competing interests.

Additional information

Extended data is available for this paper at https://doi.org/10.1038/s41592-020-0883-z.

Supplementary information is available for this paper at https://doi.org/10.1038/s41592-020-0883-z.

Correspondence and requests for materials should be addressed to W.M.

Peer review information Rita Strack was the primary editor on this article and managed its editorial process and peer review in collaboration with the rest of the editorial team.

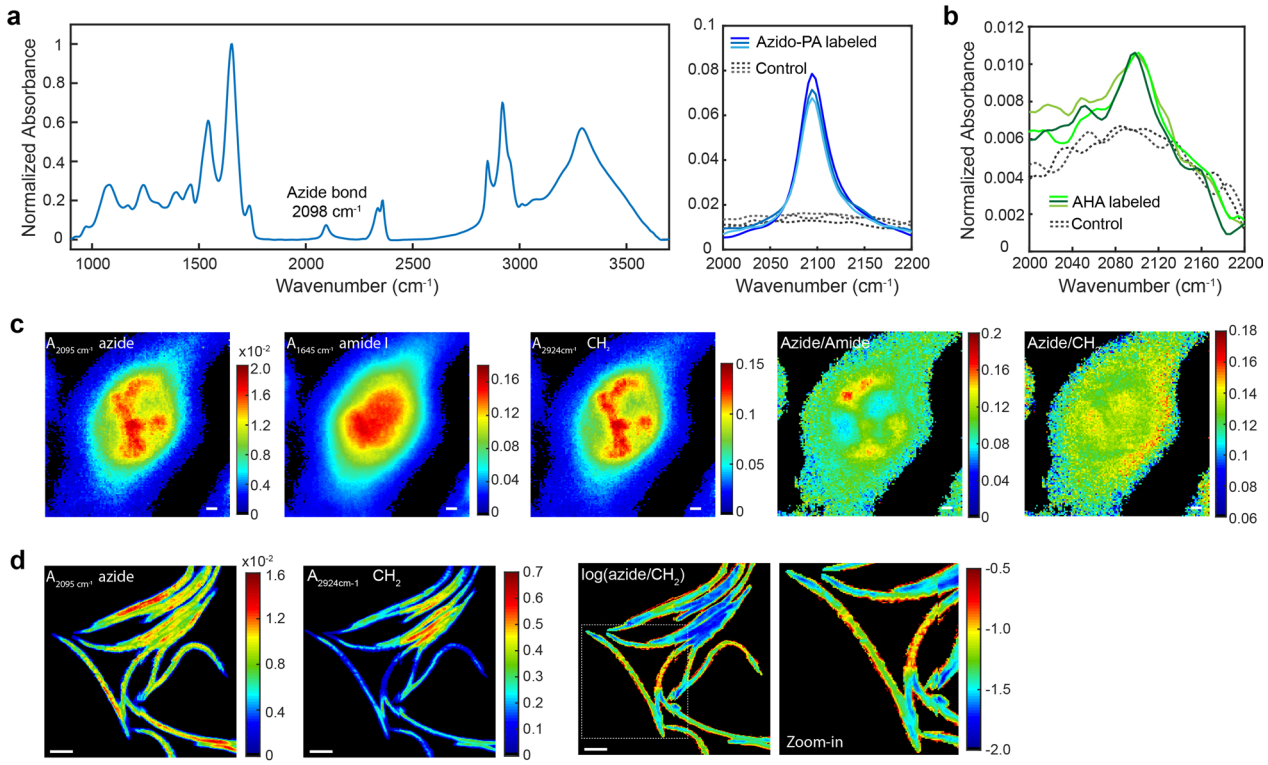

Extended Data Fig. 1 | Azide probes. A single azide band at 2098 cm^{-1} can be consistently detected on azido-palmitic acid labeled (**a**) and AHA labeled (**b**) but not on unlabeled control inside Raw264.7 cells. **c**, High-definition imaging on single azido-palmitic acid labeled Raw264.7 cells. Pixel size = 0.66 μm. The diffraction-limited resolution is about ~3 μm for the azide band. **d**, Imaging on C. elegans labeled with azido-palmitic acid. Pixel size = 3.3 μm. Experiments in **a**-**c** were repeated five times independently with similar results. Experiments in **d** were repeated three times independently with similar results. Scale bars, 5 μm in **c**, 100 μm in **d**.

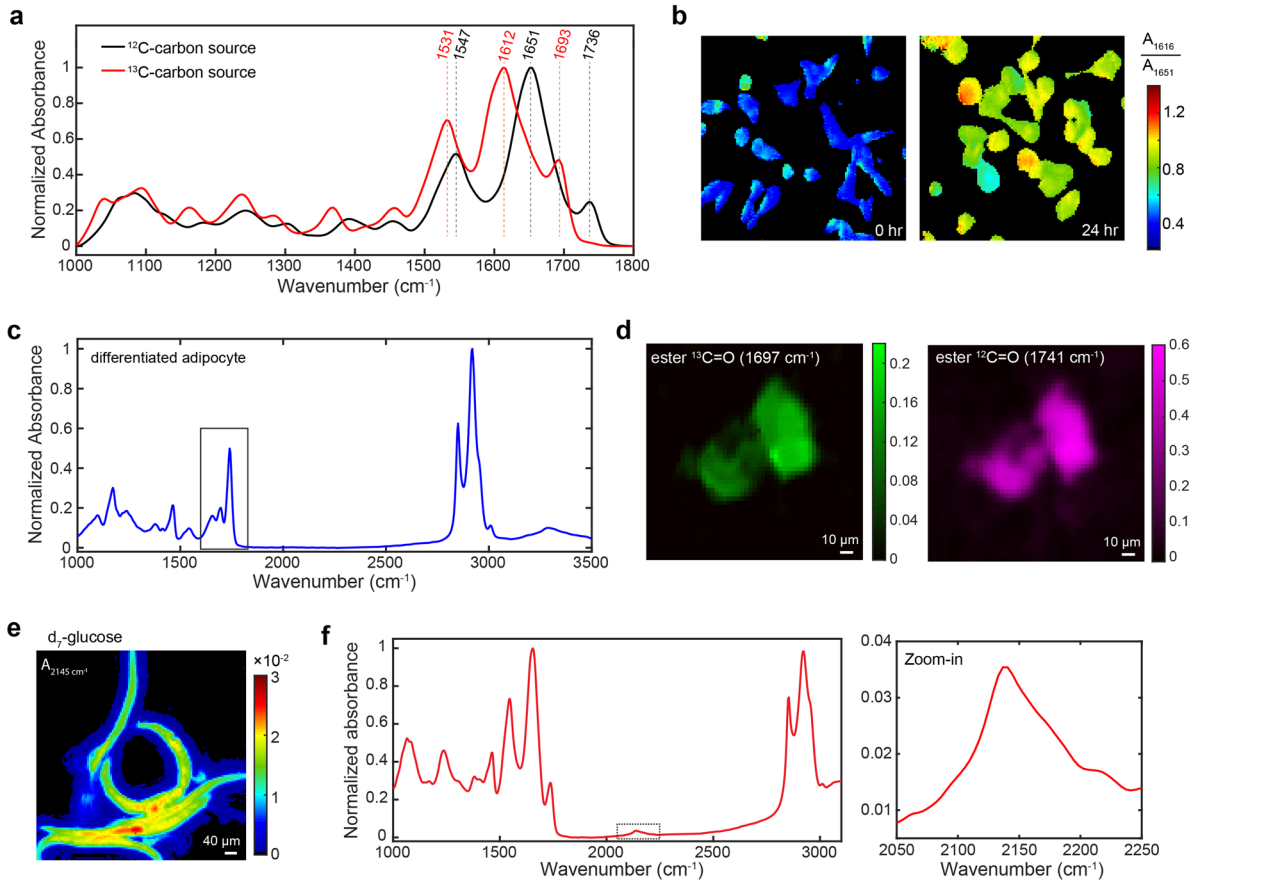

Extended Data Fig. 2 | ^{13}C-substituted precursors and carbon-deuterium probes. a, Spectral identification of ^{13}C and ^{12}C carbonyl bonds (both amide I and ester carbonyl) in bacteria grown in M9 minimum medium with $^{13}C_6/^{12}C_6$-glucose as the only carbon source. Experiments were repeated three times independently with similar results. **b**, The ratio maps as A_{1616} (absorbance at 1616 cm^{-1}) over A_{1651} increase after culturing MDA-MB-468 with ^{13}C-AA medium. Experiments were repeated three times independently with similar results. **c**, Single-pixel FTIR spectrum of differentiated adipocyte labeled with $^{13}C_6$-glucose for 4 days. The squared region was enlarged as in Fig. 1i. **d**, Imaging on de novo lipogenesis in differentiated 3T3-L1 adipocytes with $^{13}C_6$-glucose. Experiments in **c** and **d** were repeated three times with similar results. **e**, Imaging on C. elegans labeled with d_7-glucose. Experiments were repeated three times with similar results. Pixel size = 3.3 μm for **b**-**e**. **f**, Single-pixel FTIR spectrum in cerebellum of pup (P21) mice labeled with 2% d_7-glucose for 30 days (E11 to P21). The squared region (2050-2250 cm^{-1}) was enlarged in the right. Experiments were repeated on three tissue slices with similar results. Scale bars: 10 μm in **d**, 40 μm in **e**.

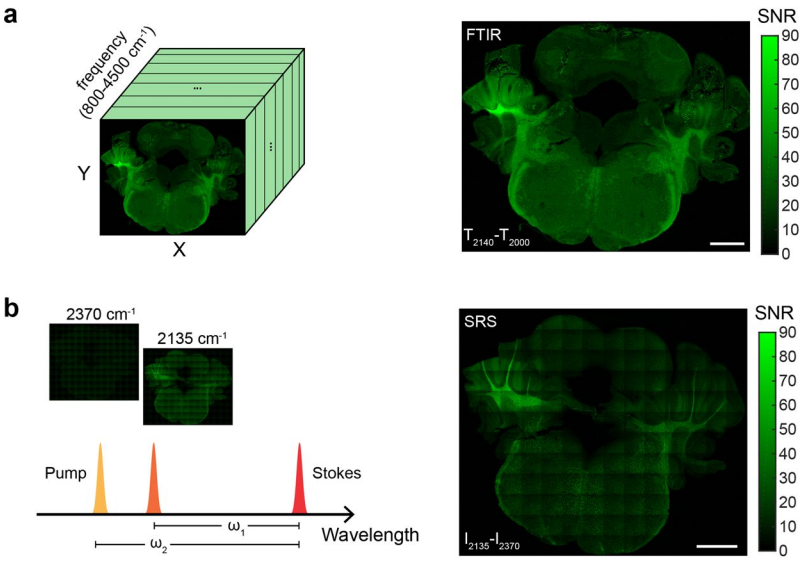

Extended Data Fig. 3 | Imaging speed comparison between broadband FTIR and single-frequency SRS. a, Broadband FTIR microscope acquires a hyperspectral data cubic in a single scan. C-D image was generated as the transmittance difference between on-resonant (2140 cm^{-1}) and off-resonant (2000 cm^{-1}) with 3.3-μm pixel size. Noise was estimated as the spectral noise in the spectral region of 2100-2200 cm^{-1}. 128 co-scans background was utilized. With 8 co-scans of signal measurement, total acquisition time is 80 min for 3.3-μm pixel size (25× objective), 30 min for 5.5-μm pixel size (15× objective) and 3 min for 20.2—μm pixel size (4× objective). **b**, Narrowband picosecond excitation was utilized in SRS microscope. C-D image was generated as the intensity difference between on-resonant (2135 cm^{-1}) and off-resonant (2370 cm^{-1}). 100-mW pump and 150-mW Stokes were utilized with 20-μs pixel dwell time and 20-μs lock-in time constant. Noise was estimated by the s.d. among pixels with only pump laser under the same laser power and lock-in time constant. Total acquisition time for a single frequency is about 20 min for 2-μm pixel size, and 80 min for 1-μm pixel size, respectively. Experiments in **a** and **b** were not repeated. Scale bars, 1 mm.

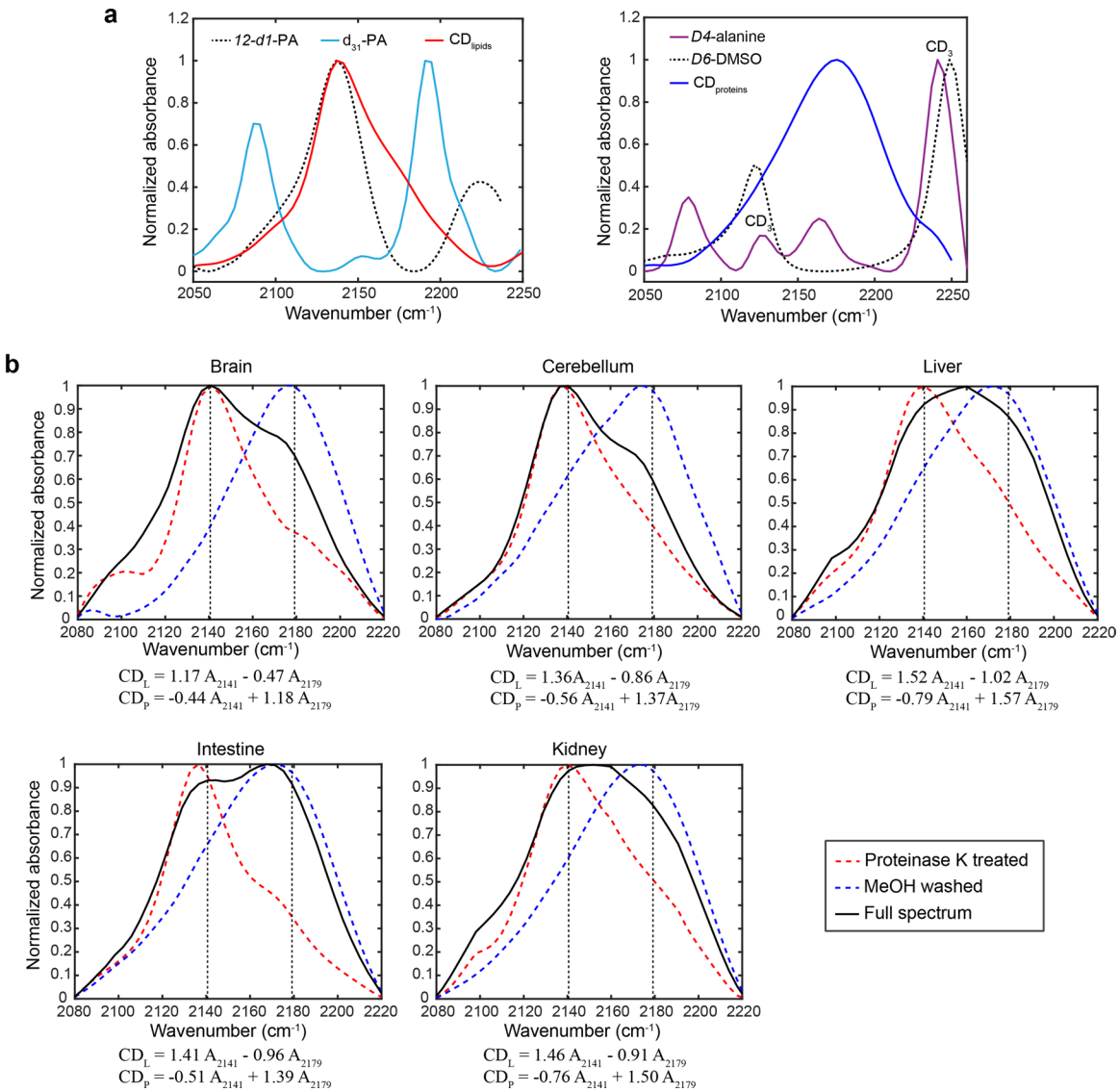

Extended Data Fig. 4 | Spectral unmixing for D_2O labeled tissues from various organs. a, Spectral characterization on CD vibrations in lipid and protein with solution standards. The isolated D-labeled lipids spectrum agrees with the CD peak in 12-**d1**-PA (left) and D-labeled protein spectrum matches with the C(α)D peak from d_4-alanine (right). Experiments were repeated two times independently with similar results. **b**, Retrieval of CD_P and CD_L signals for different organs of D_2O labeled mouse. The linear combinational algorithms for different organs are presented below each spectrum. Raw spectra were truncated to spectral region of 2080-2220 cm^{-1} followed by polynomial baseline correction and normalization. Black solid lines are spectra for untreated tissues, red dashed lines are spectra for lipid components (protein were digested with Proteinase K) and blue dashed lines are spectra for protein components (lipids were removed by methanol wash). Experiments were repeated three times independently with similar results.

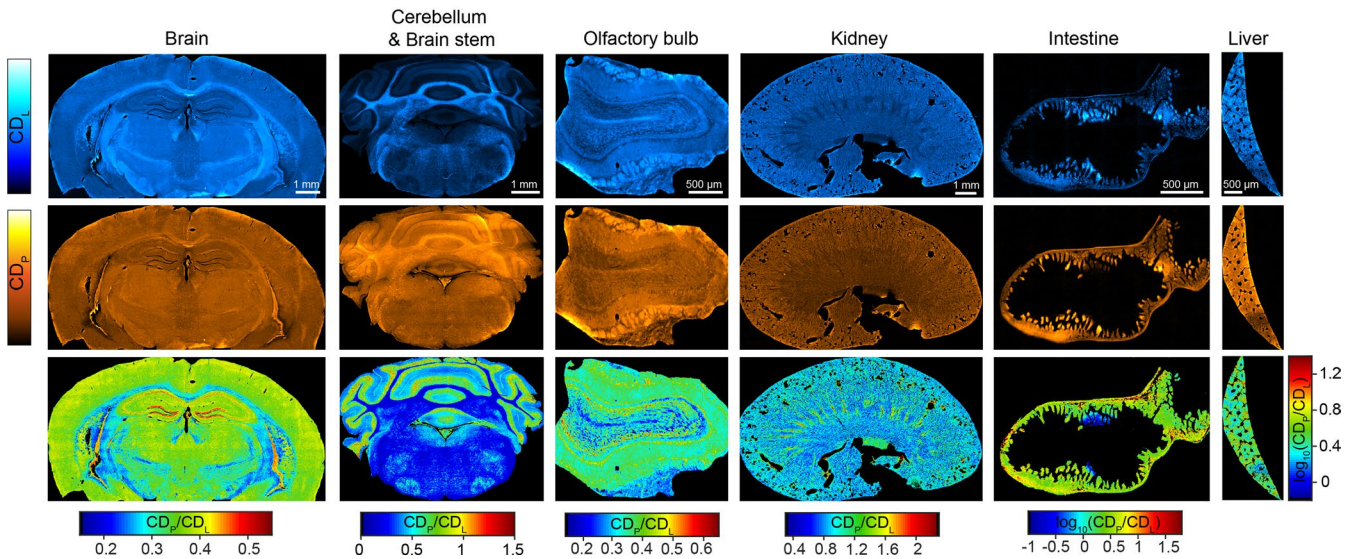

Extended Data Fig. 5 | Multiplexed imaging of macromolecules synthesis activities in D_2O labeled mice. CD_P and CD_L are D_2O-dereived protein synthesis signal and de novo lipid synthesis signal after linear unmixing (with the algorithms in Extended Data Fig. 4), respectively. Experiments were repeated on three tissue slices for each organ with similar results. Scale bars, 1mm for brain, cerebellum and kidney; 500 μm for olfactory bulb, intestine and liver.

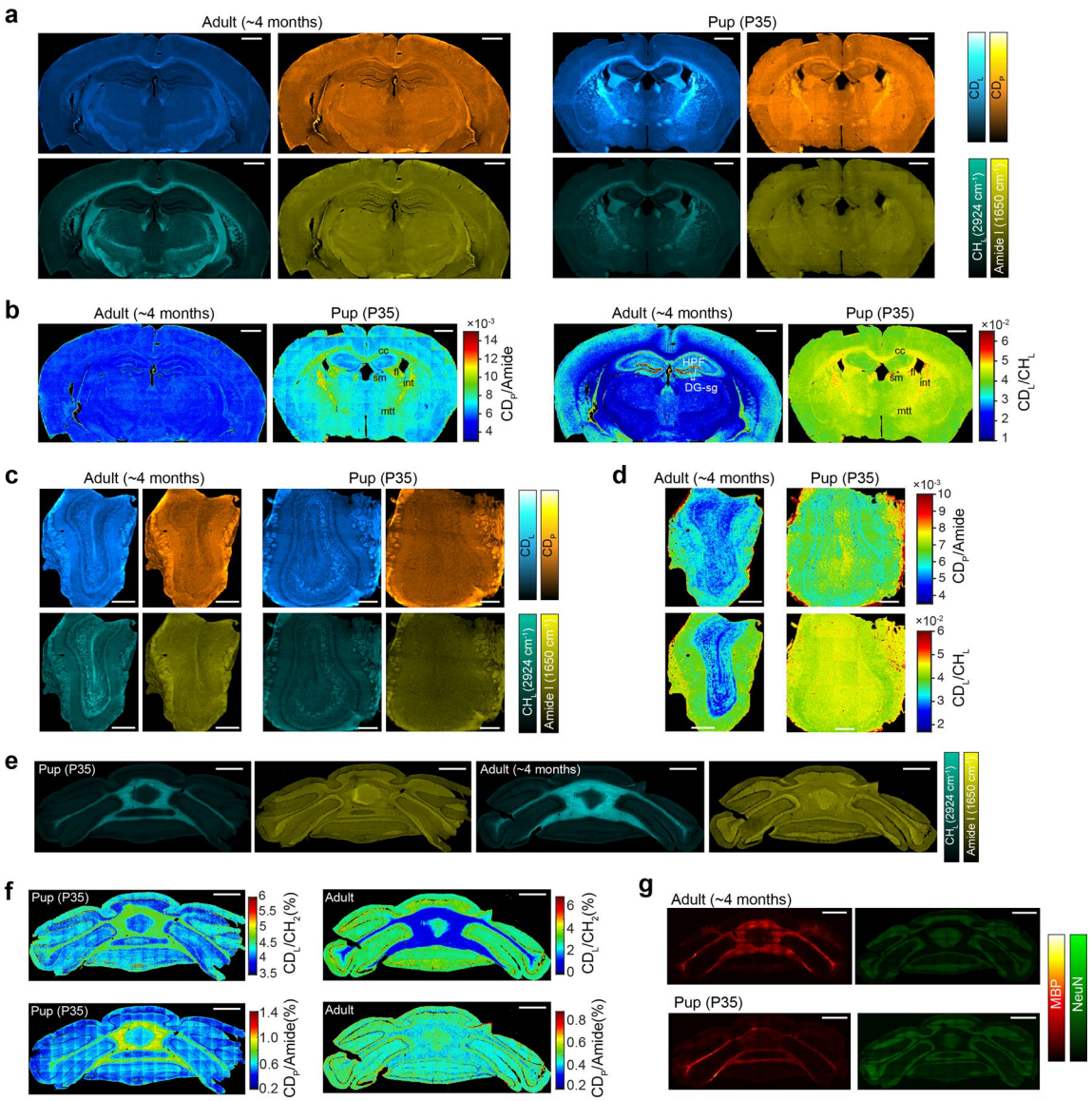

Extended Data Fig. 6 | MIR imaging of brain metabolic activities during development. a, **b**, CD_L, CD_P, Amide I and CH_L FTIR images (**a**) and generated maps of protein synthesis and de novo lipid synthesis activities (**b**) on brains of adult and young mouse. cc: corpus callosum; fi: fimbria; sm: stria medullaris; int: internal capsule; mtt: mammilothalmic tract; HPF: hippocampus; DG-sg: granule cell layer of dentate gyrus. **c**, **d**, FTIR images (**c**) and generated maps of protein synthesis and de novo lipid synthesis activities (**d**) on olfactory bulb of adult and young mouse. P35 is 35 days postnatal mice given with 25% D_2O in drinking water for P1-P35 duration and adult mice were also labeled with 25% D_2O in drinking water for 35 days. **e**, **f**, FTIR images (**e**) and generated maps of protein synthesis and de novo lipid synthesis activities (**f**) on cerebellum of adult and young mouse. Experiments in **a**-**f** were repeated on three tissue slices each with similar results. (**g**) Immunofluorescence imaging of myelin basic protein (MBP) and NeuN (neuronal nuclei) on adult and young mouse. NeuN is mainly restricted to granular layer of cerebellum. Experiments were not repeated. Scale bars, 1 mm in **a**, **b** and **e**-**g**, 500 μm in **c**, **d**.

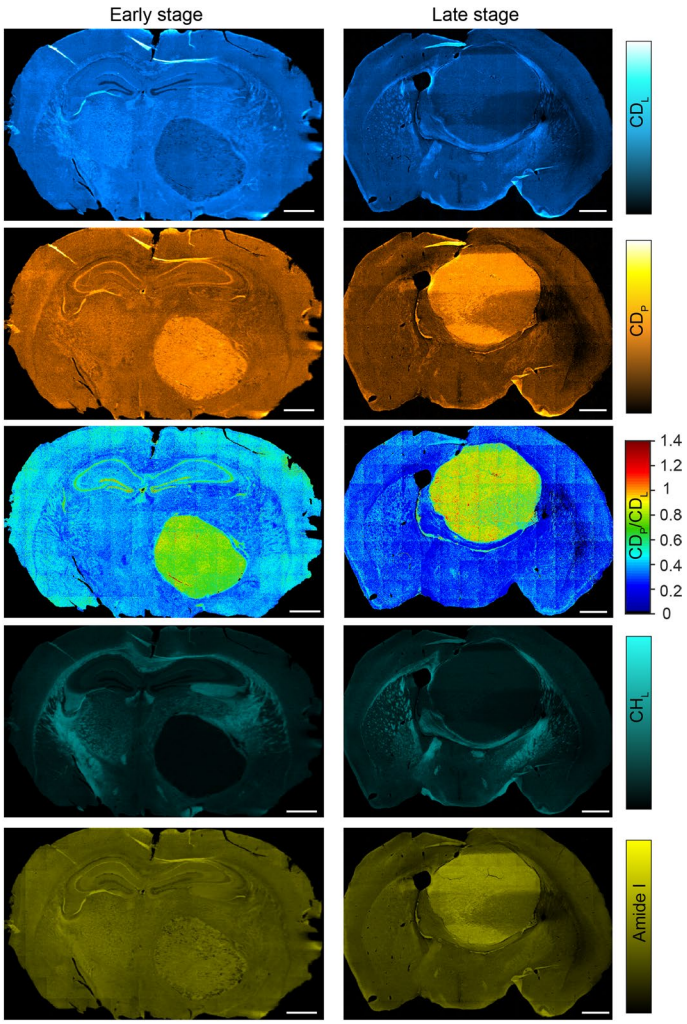

Extended Data Fig. 7 | MIR metabolic imaging on tumor progression with D_2O labeling. Left column is the early stage and right column is the late stage. Early stage: label from day 0-15 post xenograft; Late stage: label from day 11-26 post xenograft. Experiments were repeated on three tissue slices each with similar results. Scale bars: 1 mm.

nature research

Corresponding author(s): Wei Min

Last updated by author(s): May 21, 2020

Reporting Summary

Nature Research wishes to improve the reproducibility of the work that we publish. This form provides structure for consistency and transparency in reporting. For further information on Nature Research policies, see Authors & Referees and the Editorial Policy Checklist.

Statistics

For all statistical analyses, confirm that the following items are present in the figure legend, table legend, main text, or Methods section.

n/a	Confirmed	
☐	☒	The exact sample size (*n*) for each experimental group/condition, given as a discrete number and unit of measurement
☐	☒	A statement on whether measurements were taken from distinct samples or whether the same sample was measured repeatedly
☐	☒	The statistical test(s) used AND whether they are one- or two-sided *Only common tests should be described solely by name; describe more complex techniques in the Methods section.*
☒	☐	A description of all covariates tested
☒	☐	A description of any assumptions or corrections, such as tests of normality and adjustment for multiple comparisons
☐	☒	A full description of the statistical parameters including central tendency (e.g. means) or other basic estimates (e.g. regression coefficient) AND variation (e.g. standard deviation) or associated estimates of uncertainty (e.g. confidence intervals)
☐	☒	For null hypothesis testing, the test statistic (e.g. *F*, *t*, *r*) with confidence intervals, effect sizes, degrees of freedom and *P* value noted *Give P values as exact values whenever suitable.*
☒	☐	For Bayesian analysis, information on the choice of priors and Markov chain Monte Carlo settings
☒	☐	For hierarchical and complex designs, identification of the appropriate level for tests and full reporting of outcomes
☒	☐	Estimates of effect sizes (e.g. Cohen's *d*, Pearson's *r*), indicating how they were calculated

Our web collection on statistics for biologists contains articles on many of the points above.

Software and code

Policy information about availability of computer code

Data collection	FTIR data were collected with Agilent Resolution Pro software, DFIR data were collected with Daylight Solutions ChemVision software, SRS images were collected with Olympus FluoView software.
Data analysis	Image J 1.52b (image color assignment), CytoSpec v2.00.06 (FTIR data export and pre-processing) , Epina ImageLab (DFIR data export and pre-processing), CellProfiler v3.1.8 (single cell segmentation), custom MATLAB (R2016a) codes for image and single-cell analysis, GraphPad Prism 7 (statistical analysis)

For manuscripts utilizing custom algorithms or software that are central to the research but not yet described in published literature, software must be made available to editors/reviewers. We strongly encourage code deposition in a community repository (e.g. GitHub). See the Nature Research guidelines for submitting code & software for further information.

Data

Policy information about availability of data

All manuscripts must include a data availability statement. This statement should provide the following information, where applicable:

- Accession codes, unique identifiers, or web links for publicly available datasets
- A list of figures that have associated raw data
- A description of any restrictions on data availability

The authors declare that all data supporting the results in this study are available within the paper and its Supplementary Information. All raw and processed images generated in this work are available from the corresponding author on reasonable request.

Field-specific reporting

Please select the one below that is the best fit for your research. If you are not sure, read the appropriate sections before making your selection.

☒ Life sciences ☐ Behavioural & social sciences ☐ Ecological, evolutionary & environmental sciences

For a reference copy of the document with all sections, see nature.com/documents/nr-reporting-summary-flat.pdf

Life sciences study design

All studies must disclose on these points even when the disclosure is negative.

Sample size	No sample size calculation was performed. Our sample size was selected for adequately demonstrating the technical performance of our probes under the context of infrared metabolic imaging, with considering previous Raman studies in a relevant design (Zhang et al. Nat Biomed Eng, 2019 and Shi et al. Nat Comm, 2018).
Data exclusions	No data were excluded.
Replication	Three replicate were usually performed for cell-culture experiments with independent measurement and analysis. The results were reproducible.
Randomization	For mice experiments, newborn mice (postnatal 14–35 days old) and adult mice (3–5 months old) were separated into the two age groups.
Blinding	Blinding was not pertinent to this study. For experiments to study new born and adults mice, it is not necessary to blind the group because the experiments were designed to study metabolic activity difference of newborn and adult mice.

Reporting for specific materials, systems and methods

We require information from authors about some types of materials, experimental systems and methods used in many studies. Here, indicate whether each material, system or method listed is relevant to your study. If you are not sure if a list item applies to your research, read the appropriate section before selecting a response.

Materials & experimental systems

n/a	Involved in the study
☐	☒ Antibodies
☐	☒ Eukaryotic cell lines
☒	☐ Palaeontology
☐	☒ Animals and other organisms
☒	☐ Human research participants
☒	☐ Clinical data

Methods

n/a	Involved in the study
☒	☐ ChIP-seq
☒	☐ Flow cytometry
☒	☐ MRI-based neuroimaging

Antibodies

Antibodies used	Commercial primary antibodies: rat anti-myelin basic protein antibody (Abcam, Cat# ab7349, monoclonal [12], used at 1:200) rabbit anti-NeuN (Invitrogen, Cat# PA5-78639, polyclonal, used at 1:500) Commercial dye-conjugated secondary antibodies: Donkey anti-Rabbit-Alexa568 IgG (H+L) (Invitrogen, Cat# A10042, used at 1:500) Donkey anti-Rat-Alexa488 IgG (H+L) (Abcam, Cat# ab150153, used at 1:500)
Validation	Antibodies were validated by the manufacturer. anti-myelin basic protein antibody: tested suitable for IHC/IF with species reactivity with mouse on abcam website. See relevant citation on PubMed: 23584610 (Yang et al., Nat Biotech 2013) anti NeuN: tested suitable for IHC/IF with species reactivity with mouse on Thermo Fisher website. RRID: AB_2736207.

Eukaryotic cell lines

Policy information about cell lines

Cell line source(s)	Cell lines were purchased from ATCC including HeLa (ATCC CCL-2), Raw264.7 (ATCC TIB-71), MDA-MB-231 (ATCC HTB-26), MDA-MB-468 (ATCC HTB-132), MCF7 (ATCC HTB-22), 3T3-L1 MBX (ATCC CRL-3242) and U-87 MG (ATCC HTB-14).

Authentication	ATCC authenticated the cells.
Mycoplasma contamination	Cell lines were not tested for mycoplasma contamination.
Commonly misidentified lines (See ICLAC register)	No commonly misidentified cell lines were used.

Animals and other organisms

Policy information about studies involving animals; ARRIVE guidelines recommended for reporting animal research

Laboratory animals	Mice of strain C57BL/6J and strain J:NU were used in this study. Postnatal mice were 14-35 days old, and adult mice were 3-5 months old. All adult mice were female. Postnatal mice were male and female.
Wild animals	The study did not involve wild animals.
Field-collected samples	The study did not involve samples collected from the field.
Ethics ove	